Fine characterization of the capillary instability of free viscoelastic jets

Christophe Dumouchel, Louise Cottier, Marie-Charlotte Renoult

To cite this version:

Christophe Dumouchel, Louise Cottier, Marie-Charlotte Renoult. Fine characterization of the capillary instability of free viscoelastic jets. Journal of Non-Newtonian Fluid Mechanics, 2023, 322, pp.105135. 10.1016/j.jnnfm.2023.105135 . hal-04257771

Fine characterization of the capillary instability of free viscoelastic jets

Christophe Dumouchel[1], Louise Cottier, Marie-Charlotte Renoult
CNRS – CORIA-UMR 6614, Normandie Univ, UNIROUEN, INSA Rouen
76801 Saint-Etienne du Rouvray, France

Abstract:
The experimental approach presented in this article investigates low-velocity small-diameter cylindrical viscoelastic jets. It consists in producing and analyzing sets of jet portion images taken at different positions along the jet axis, i.e., from the nozzle producing the jet down to the spray region. A very significant part of the work was dedicated to develop analyzing tools: a proper orthogonal decomposition to identify the onset of the capillary instability, a procedure to determine the mean jet breakup length and a multi-scale tool to describe the jet local shape and its evolution along the jet axis. Used in a similar previous study, the multi-scale analysis has been extended in the present work. These tools are shown to be well suited to the experimental study conducted here, and in particular to meet the need for statistical analysis that free jets impose. They are applied to study the capillary instability of free jets of dilute polyethylene oxide solutions produced from a micrometer nozzle. The parameters of the study are the molar mass of the polymer and the velocity of the jet. Results on the detection of the capillary instability onset, the jet evolution dynamics towards the Bead On A String (BOAS) pattern, the local extensional relaxation time and the terminal elongational viscosity of the solutions, the bead coalescence mechanism and its influence on the size of the spray drops are obtained. Analysis of these results reveals that the polymers undergo two episodes of mechanical degradation during the process: the first one at injection, the second one during the elasto-capillary regime of the jet breakup. Moreover, the scenario in the literature suggesting a sufficiently relaxed axial tension of the flow for the capillary instability to occur is found to be not always valid. It is also shown that the average size of the drops correlates with the intensity of the bead coalescence mechanism that takes place on the BOAS. These results demonstrate the richness of the adopted approach and in particular of the multi-scale analysis to study the development of a fluid interfacial instability.

***Keywords**: Jet break-up, Dilute polymer solution, Instability, Multi-scale analysis, Proper Orthogonal Decomposition, Polymer mechanical degradation*

1 - Introduction

Liquid jets produced by a circular nozzle into ambient air are the subject of numerous theoretical, numerical and experimental studies (see Eggers and Villermaux (2008) for a comprehensive review). These flows are particularly interesting because there are subjected to a

---

[1] Corresponding author: christophe.dumouchel@coria.fr, 00 33 2 32 95 36 23

capillary instability that leads to the breakup of the jet into a succession of drops, i.e., a spray. The understanding of this fundamental liquid atomization process is necessary to improve the prediction and control of the sprays. As far as this seond point is concerned, adding a minute amount of polymer in a simple liquid such as water or oil, and doing so conferring viscoelastic properties to the fluid, is a track under study to control spray characteristics (Christanti and Walker, 2001). The present work is precisely dedicated to the experimental study of the behavior of cylindrical jets of dilute polymer solutions with sufficiently small diameter and velocity so that their behavior is not affected by aerodynamic forces. The produced jets are free, i.e., they are not subjected at the nozzle to any imposed disturbances.

As for Newtonian jets (Leib and Goldstein 1986; Blaisot and Adeline 2003), just outside the nozzle, a distance over which viscoelastic jets show no visible disturbance was reported (Christanti and Walker 2001; Tirel 2019). Preceding the onset of the capillary instability, this neutral regime (NR) depends on the relaxation of the velocity profile but also, in the case of viscoelastic jets, on a stabilizing tensile stress to which they are subjected (Gill and Gavis 1956; Gavis and Gill 1956; Gavis and Middleman 1963; Entov 1988). The onset of the capillary instability marks the end of this neutral regime. Several experimental studies on free viscoelastic jets determined the wavelength and growth rate of this capillary instability and the breakup length of the jets (Mun et al 1998, Christanti and Walker 2001, Charpentier et al. 2017, Brenn and Stelter 2020). Performing measurements in the early stage of the capillary instability in jet experiments of low-viscosity dilute polymer solutions, Charpentier et al. (2017) obtained wavelength and growth-rate values close to those obtained for Newtonian jets of the solutions solvent. The initial stage of the jet dynamics characterized by a sinusoidal growing disturbance is an Inertia Capillary Regime (ICR) during which the capillary forces are balanced by inertia forces and the elastic contribution of the polymer is not yet sufficient to affect the flow. However, the breakup lengths are very much affected by the presence of polymers, even for the case of low-viscosity dilute polymer solutions. This length is found to increase as the molar mass of the polymer or/and the polymer concentration increases (Mun et al 1998, Christanti 2001, Brenn and Stelter 2020).

The increase of breakup length is due to the elastic contribution of the polymers whose effect can be seen in a significant change of the shape of the jet. The growing disturbance is not sinusoidal anymore and the formation of a succession of beads connected by strings and called Bead On A String (BOAS) pattern takes place (Entov and Yarin 1984, Yarin 1993). The extensional flow in the strings or ligaments expels liquid towards the beads following two successive thinning regimes: an Elasto-Capillary Regime (ECR) and a Finite Extensibility Regime (FER). During the ECR, the liquid drainage is controlled by the elastic forces caused by the polymer uncoiling process. During the FER, the polymer uncoiling process is over and the liquid drainage is controlled by visco-elastic forces. These dynamics are not affected by the bead coalescence mechanism, which refers to a bead sliding downstream or upstream along the ligaments of the BOAS pattern until it meets another bead and coalesce with it (Li and Fontelos, 2003). However, the coalescence mechanism must have an effect on the size of the spray drops. Of course, the ECR and FER depend on the viscoelastic properties of the solution. But these properties depend on the injection.

Indeed, injection of polymer solutions through small dimension orifices induces mechanical degradation which refers to scission of the macromolecules. The condition for this mechanism to occur is related to the internal flow characteristics (Culter et al. 1975, Merrill and Leopairat 1980, Nguyen et al. 1988, Odell et al. 1990, Nghe et al. 2010, Rognin et al. 2021). Polymer degradation induces a decrease of polymer molar mass, of extensional relaxation time and of terminal elongational viscosity of the solution. Note that, if the mechanical degradation of polymers generated by injection has benefitted from numerous studies, the mechanism during atomization processes as mentioned by Yarin (1993), Stelter et al. (2000) or Gaillard et al. (2022) has received far less attention. Yet, simple estimates of the magnitude and duration of elongational strain and strain rate during the ECR indicate that the conditions for chain scission are present.

The study presented here involves the measurement of the characteristic properties of the capillary instability (onset of instability, wavelength, growth rate, jet breakup length) as well as the in-situ measurement of the viscoelastic properties of the solutions (extensional relaxation time and terminal elongational viscosity) for free jets of dilute polymer solutions. These measurements are obtained by analyzing the shape of the jets during the instability process. To ensure accurate shape detection, the jets are imaged by portions rather than along their entire length, and the optical system arrangement is selected to provide a very fine spatial resolution. Specific tools are developed to perform analyses that have to be statistical since the jets are free. A proper orthogonal decomposition measures the average distance at which the capillary instability begins. A specific procedure to determine the jet breakup length is developed to overcome the lack of global jet visualizations. As far as the analysis of the shape of the jet is concerned, a multi-scale description tool is applied.

When the jet perturbation is sinusoidal, the measurements of the maximum and minimum jet diameters as well as of the perturbation wavelength provide a complete jet shape description. However, this is not the case anymore when the perturbation is not sinusoidal as, for instance, when the present jet ECR is approached. The multi-scale tool used in this work allows a complete description of the jet shape whatever it is. In a previous application on viscoelastic jets, Tirel et al. (2020) showed that this method is adapted to statistical approaches, and, taking inspiration from the literature (Schümmer and Tebel, 1983; Keshavarz et al. 2015, Sharma et al. 2015, Matheus et al. 2018), it allows measuring an extensional relaxation time from free viscoelastic jet experiments. This extensional relaxation time was obtained from the temporal evolution of a mean scale identified by the multi-scale tool and whose decrease dynamics was demonstrated to be the same as that of the mean diameter of the ligaments seen at a given position in the ECR. Furthermore, it was demonstrated that the decrease dynamics of the mean diameter of an ensemble of ligaments of varying size is the same as that of each individual ligament provided that they all have the same thinning ligament dynamics and extensional relaxation time. Compared with the previous work (Tirel et al. 2020), the multi-scale analysis has been improved thanks to a slightly better optical spatial resolution and a larger number of images. In addition, it is extended to the determination of perturbation wavelengths, of drop size distribution and of bead coalescence mechanism. The wavelength estimation procedure is possible thanks to a recent theoretical contribution concerning this description tool (Dumouchel et al. 2022).

Thanks to the development of these tools, the present analysis focuses on three main aspects: the link between axial tension and the onset of the capillary instability, the detection and influence of the polymer degradation mechanism during the instability and the link between bead coalescence and drop size. The polymer molar mass and the jet velocity are the parameters of this experimental investigation.

2 - Experimental setup, operating conditions and image processing

2.1 - Experimental setup

The experimental setup used to produce vertical free liquid jets and to visualize them is described in Tirel et al. (2020). It is summarized here and emphasis is placed on the improvements or differences.

Fed by a syringe-pump (Chemyx Nexus 6000), the injector has a cylindrical body (D_{in} = 5 mm internal diameter, L_{in} = 85 mm length) and ends with a disc with a circular hole in the center. This hole is the injector nozzle. Its diameter and length are: D_{or} = 200 µm and L_{or} = 300 µm.

The optical visualization system is a backlight imaging assembly. The light source is a cavitar laser source (Cavilux Smart 400W). The camera (Baumer LXG-500M, 7920 x 6004 pixels), which is different from the one used in Tirel et al. (2020), is equipped with a long-distance microscope (Infinity K2 DistaMax). This system offers a slightly better spatial resolution than in Tirel et al. (2020). The visualized physical field covered by the optical arrangement is 9.623 mm x 7.295 mm corresponding to a spatial resolution equal to 1.215 µm·pixel^{-1}. The injector is placed vertically on a 3D displacement system (200 mm vertical rise, ZABER T-LSM 3-D system) allowing the jet to be focused and visualized at different vertical positions under the injector without modifying the optical arrangement. The vertical offset between two consecutive positions is 8 mm. At each position, a large number of images (around 600) uncorrelated in time are taken for statistical analysis. This number is four times larger than in Tirel et al. (2020). The camera sensor exposure and the light source are synchronized by a TTL signal generator and the image frame rate is set at 5 Hz. The short light pulse duration (20 ns) ensures freezing the jet on the image.

In the following, the downstream distance from the nozzle exit is noted z.

2.2 - Operating conditions

The experimental work is conducted with four dilute polymer solutions made with PolyEthylene Oxide (PEO) polymers of four different molar masses M ({0.6; 1; 5; 8}x10^{3} kg·mol^{-1}) and provided by Sigma-Aldrich. For concision, they will hereafter be referred to in the text as S06, S1, S5 and S8, respectively. The solvent is a mixture of water and isopropyl alcohol (95-5 in weight percent respectively, shear viscosity η_s = 1.1 mPa·s). The mass fraction of PEO in the solvent is 5 ppm (0.5x10^{-3} %) for all four solutions. In the study of Tirel et al. (2020) all solutions were made with PEO of molar mass M = 8x10^{-3} kg·mol^{-1} but at several concentrations. After preparation, solutions are stored in the refrigerator for 72 hours to freely homogenize. They are taken out the day before the experiments, to be at room temperature. The solutions density ρ_L, shear viscosity η_L and surface tension with air σ, measured at 24°C (room temperature) with a densimeter (Anton Paar DMA 35), rotational viscosimeter (Anton Paar MCR 302e) and tensiometer (Lauda TVT 2), respectively, are reported in Table 1. These solutions can be considered as Boger solutions and therefore show negligible shear-thinning effects. The solution ratios c/c^* estimated as $(\eta_L - \eta_s)/\eta_s$ (Larson, 2005) and given in Table 1 indicate that the solutions are dilute.

The relaxation time of the solutions are evaluated with the Zimm model that describes the behavior of the polymeric chains in dilute polymer solutions, considering the hydrodynamic interactions with the solvent (Doi and Edwards, 1988). The Zimm relaxation time t_{RZ} can be expressed as:

$$t_{RZ} = \frac{\eta_s N'^{3\upsilon} b^3}{M'^{3\upsilon} k_B T} M^{3\upsilon} \tag{1}$$

where M' is the monomer molar mass, N' is the number of monomer main elements, b is the effective bond length of these elements, k_B is the Boltzmann constant and T is the temperature. Here, $M' = 44.06$ g·mol^{-1}, $N' = 3$, $b = 146.4$ pm and $T = 297$ K. The exponent υ, known as the Flory coefficient, is a constant and according to the literature is equal to 0.588 (Cotton 1980). The solution Zimm relaxation time are given in Table 1.

	S06	**S1**	**S5**	**S8**
Polymer molar mass M (10^3 kg.mol^{-1})	0.6	1	5	8
Density ρ_L (kg/m^3)	988	988	988	988
Shear viscosity η_L (mPa.s)	1.14	1.21	1.17	1.23
Surface tension σ (mN.m^{-1})	42.0	46.5	46.3	46.5
c/c^*	0.036	0.100	0.034	0.118
t_{RZ} (ms)	0.11	0.28	4.83	11.1

Table 1: Physical and rheological properties at 24°C of the solutions.

The syringe pump flow rate Q_{vc} ranged from 13.2x10^{-8} m^3·s^{-1} to 23.8x10^{-8} m^3·s^{-1} in the present work. For each case, the effective flow rate Q_v issuing from the injector is systematically measured by weighting the amount of liquid collected during a controlled time interval. A mean velocity V_{or} is calculated from Q_v. A series of characteristic dimensionless numbers are calculated and given in Table 2: a Reynolds number $Re = \rho_L V_{or} D_{or}/2\eta_L$, a Weissenberg number $Wi = 2t_{RZ}V_{or}/D_{or}$, a Weber number $We = \rho_L V_{or}^2 D_{or}/(2\sigma)$, an Ohnesorge number $Oh = \eta_L/(\rho_L \sigma D_{or}/2)^{0.5}$ and a Deborah number $De = (8t_{RZ}^2\sigma/(\rho_L D_{or}^3))^{0.5}$. The nozzle internal flow maximum strain rate $\dot{\varepsilon}_{inj} = 1.28V_{or}/D_{or}$ (James and Saringer, 1982) are also gathered in Table 2.

According to James and Saringer (1982), the Reynolds numbers and maximum strain rates reflect the presence of a secondary flow upstream the nozzle entrance. Cartelos and Piau (1992) visualized such secondary flows for injector geometry similar to the one used here and mentioned the dependence of its development on the polymer molar mass. The Reynolds numbers indicate that the jets are laminar and, considering that the injection is performed in air, the small Weber numbers demonstrate the absence of aerodynamic effects. Finally, the Weissenberg and Deborah numbers show that viscoelastic effects are expected small for S06 and S1 compared to S5 and S8.

	S06	**S1**	**S5**	**S8**
Reynolds number *Re*	[314; 616]	[363; 627]	[350; 630]	[337; 610]
Weissenberg number *Wi*	[4; 7.8]	[12; 22]	[200; 361]	[466; 842]
Weber number *We*	[31; 120]	[42; 125]	[36; 120]	[37; 122]
Ohnesorge number *Oh*	0.018	0.018	0.017	0.018
Deborah number *De*	0.72	1.92	33	75
Internal flow maximum strain rate $\dot{\varepsilon}_{inj}$ (x10^3s^{-1})	[23; 45]	[28; 49]	[26; 48]	[27; 49]

Table 2: Range of dimensionless numbers and internal flow maximum strain rate.

2.3 - Image processing

The processing steps of the raw images are in all respects identical to those of the previous study (Tirel et al., 2020). The first step deletes the background inhomogeneity. The second step segments the image in a two-level image first, by detecting the liquid objects on the image, and second, by segmenting each object with a local intensity threshold (see Tirel et al., 2020 for more details). After this step, the liquid appears in black on a white gas phase and the images are ready to be analyzed.

The analysis of the jets is statistical and local. The statistical character is ensured by the use of a large number N_t of images (ranging from 600 to 620 according to the operating conditions). The local character results from the analysis of the jets by portions that are delimited by a rectangular Analysis Window (AW) whose height is 1 mm. At a given position, the N_t jet portions delimited by the AW constitute a local jet sequence on which the analyses presented in the next section are conducted. To analyze the jet over its entire length, the AW position (distance between the nozzle exit and the AW median line) varies from the injector down to the spray region. The vertical offset of the AW is 0.5 mm. For the longest jet in this study, there are 98 AW positions.

3 - Analysis tools and measurement techniques

3.1 – Proper Orthogonal Decomposition (POD) analysis

A POD analysis is proposed to identify the onset of the capillary instability on the jet. It is inspired by a work due to Yon et al. (2004).

The POD is a linear decomposition of a data system in a base of orthonormal vectors. The eigenvectors of this base are found by optimizing the projections of the system on it (Berkooz et al. 1993). The eigenvectors associated with the greatest eigenvalues are those that provide the best representation of the system. Therefore, they allow extracting the main system features and provide a much lower-dimensional description of it. In the present case, the high-dimensional system consists of a large number N_t of images, uncorrelated in time, showing N_t realizations of the jet portion at the same downstream position. Each image i is transformed into a vector I_i whose coordinates are the gray level values of each pixel in the image. The POD returns the base of orthogonal eigenvectors ϕ_k such that:

$$I_i = \sum_{k=1}^{N_t} a_{ik}\phi_k \qquad \text{for } i = 1,\ldots, N_t \tag{2}$$

where a_{ik} are the reconstruction coefficients. In the present application, the vectors ϕ_k of the new base can then be transformed as images, referred hereafter as eigenmodes. Their role in the reconstruction of the entire series is measured by the energy $E(\phi_k)$ which, in percentage, is expressed by:

$$E\left(\phi_k\right) = 100\frac{\sum_{i=1}^{N_t} a_{ik}^2}{\sum_{n=1}^{N_t}\sum_{m=1}^{N_t} a_{nm}^2} \tag{3}$$

By construction, the eigenmode energy $E(\phi_k)$ decreases with increasing index k.

The POD analysis was performed on the local jet sequences. Before the analysis, it is necessary to set the jet axis on the same pixel line from one image to the next, so that positional variation is not included in the POD analysis. Based on a maximum of 400 images per series (found to be sufficient for reaching convergence), the POD analysis was performed on successive local jet sequences along the direction z.

At a position where the capillary instability is visible, the shape of the jet is different from one image to another. In terms of POD analysis, this means that more than one eigenmode is required to represent the system of jet images. In another hand, at a position where no capillary instability is visible, the shape of the jet does not change from one image to another and the POD reports one eigenmode only. This is expected to be the case in the neutral regime where the jet shape is stationary. Thus, considering the energies of the first eigenmodes allows identifying the onset of the capillary instability. As an example, Fig. 1 shows the three first eigenmode energies as a function of the downstream distance z for S8 at $We = 49$. In the near injector region, $E(\phi_1)$ is constant and almost equal to 100 %, whereas $E(\phi_2) \approx E(\phi_3) \approx 0$. Further downstream, $E(\phi_1)$ starts a continuous decrease while $E(\phi_2)$ and $E(\phi_3)$ both increase. The limit between these two behaviors corresponds to the axial position Z_{onset} at which the capillary instability starts. This limit is determined by fitting the $E(\phi_1)$ function (see Fig. 1) and by extracting from the fit the position z for which $E(\phi_1)$ is equal to 99.95% of the constant $E(\phi_1)$ value of the near injector region. For the case presented in Fig. 1, $Z_{onset} = 10.8$ mm. Smaller z positions belong to the jet neutral regime.

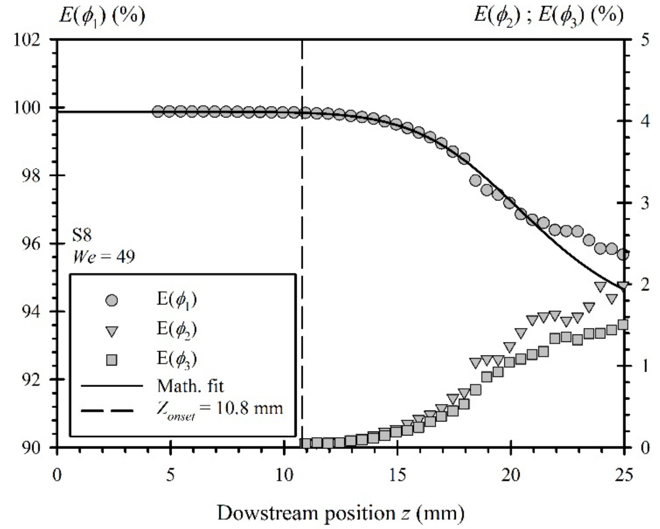

Figure 1: Energies $E(\phi_1)$ $E(\phi_2)$ and $E(\phi_3)$ of the three first eigenmodes and determination of Z_{onset}. S8, $We = 49$.

3.2 - The breakup length measurement

The breakup length is the distance between the nozzle exit section and the first point at which the jet has entirely pinched-off. The measurement of this length does not pose any difficulty when the liquid jet is fully visualized, but this is not the case in this work where the jets are visualized by portions. Furthermore, since the jet is free rather than forced, the breakup length is not constant over time and may vary significantly from moment-to-moment, so the point of breakup may or may not be present in consecutive frames of the local jet sequences in the breakup region. To access to the jet breakup-length distribution, the following procedure was developed.

For each local jet sequence, the number of images where at least one jet breakup event is observed is counted. The evolution of this number with the distance from the injector nozzle corresponds to the cumulative of the breakup length distribution. This is all the more true for viscoelastic jets since the presence of liquid ligaments after jet rupture is highly unlikely. Indeed, due to elastic forces, any rupture implies the immediate contraction of the detached element into a drop and negates the presence of ligamentous structures downstream the rupture. Since in the spray region, the number of images reporting a rupture is N_t, the total number of images of the local jet sequences, and the measured cumulative breakup length distribution can be fitted by the following function:

$$F_{BU}\left(z\right)=\frac{N_t}{1-\left(\frac{z}{E}\right)^{-h}} \tag{4}$$

where the positive parameters E and h that ensured the best fit with the measurements were determined with a Python routine. Very good fits were obtained. The breakup length distributions calculated as the derivative of $F_{BU}(z)$ are mono-modal and symmetric with a peak positioned at $z = E$, which corresponds to the arithmetic mean breakup length noted L_{BU}.

3.3 - Multi-scale analysis

The multi-scale analysis is an image analysis approach that consists in considering the liquid system as well as all systems parallel to it in the liquid phase. The parallel systems are those obtained by erosion operations performed at all possible scales, i.e. until the liquid system has been totally eroded. The erosion operation at scale d is a classic image analyzing tool. It consists in removing the liquid system region covered by a disk of diameter d that has been dragged along the interface keeping the circle center on the interface line. The smallest scale that leads to total erosion of the system is the maximum scale and is denoted d_M. As an example, a circle of diameter D eroded at scale d is a circle of diameter $(D - d)$. Since both circles have the same center, they are said parallel with each other. The scale $d = D$, is the smallest one that totally erodes the circle. Therefore, $d_M = D$.

Imaged in 2D, the liquid system and its parallel systems are described by their surface area $S(d)$, their circumference $L(d)$ and their length-integrated-curvature $H(d)$:

$$H(d) = \int_{L(d)} \kappa(d)\, dl \tag{5}$$

$\kappa(d)$ is local curvature of the eroded system at scale d. $S(0)$, $L(0)$ and $H(0)$ characterize the liquid system. It has been demonstrated (Dumouchel et al. 2022) that the way $S(d)$, $L(d)$ and $H(d)$ connect with each other depends on whether the erosion scale d is smaller or greater than a specific scale called the reach of the system and named d_R. Thanks to surface tension effects, liquid system boundaries are always smoothed and do not show tips. For small erosion scales, the parallel system boundaries are still smoothed. However, for large erosion scales, the parallel system boundaries are not smoothed anymore and show tips. These tips are called cusps. The smallest scale for which the erosion operation reports at least one cusp is the reach d_R of the system. Within the scope of this work, attention focuses on the reach d_R and on the maximum scale d_M. For a liquid jet disturbed by a sinusoidal perturbation, the reach is the pinch-off diameter of the jet and the maximum scale is the jet diameter at a swelling. For a BOAS structure, the reach corresponds to the ligament diameter and the maximum scale to the bead diameter.

The appendix presents the application of the theoretical elements to a 2D representation of a portion of a liquid jet disturbed by a sinusoidal perturbation (Dumouchel et al. 2022). This application provides a theoretical expression for the derivative $L(d)_{,d}$ where $\bullet_{,d}$ denotes the derivative w.r.t. d. Two numerical applications are shown in Fig. 2 with the radius of the unperturbed column a = 100 [L] (arbitrary unit of length), the wavelength λ = 800 [L] and the perturbation amplitude Ap = 10 and 20 [L]. The application concerns a one λ-long column leading to a number of cusps $n = 2$ for all scale d. The reach of these systems is $d_R = 180$ [L] and 160 [L] and the maximum scale $d_M = 220$ [L] and 240 [L] for the smallest and largest amplitude, respectively. For the erosion scales less than d_R, we note in Fig. 2 that $-L(d)_{,d}$ remains equal to zero because, like the liquid system, the eroded systems are homeomorphic to a 2D-cylinder (Dumouchel et al. 2022). Beyond the reach, the function $-L(d)_{,d}$ shows two discontinuities at d_R and d_M.

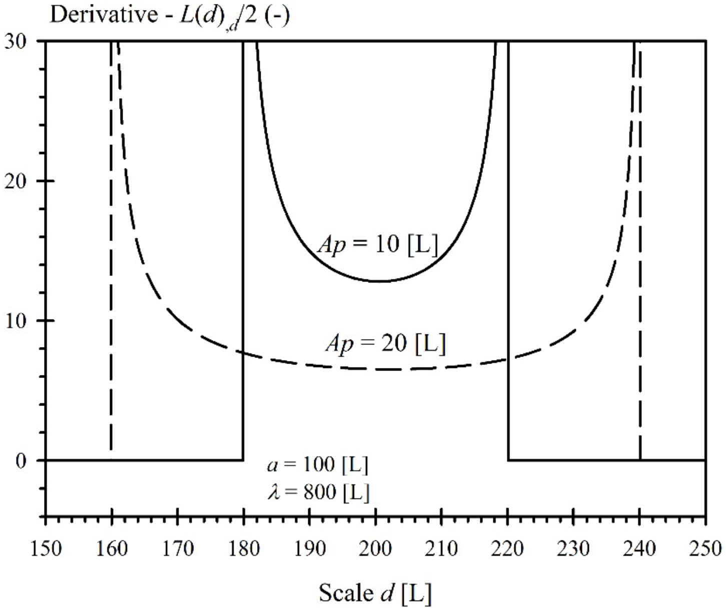

Figure 2: Examples of $-L(d)_{,d}/2$: $a = 100$ [L], $\lambda = 800$ [L], $n = 2$, solid line $Ap = 10$°[L], dashed line $Ap = 20$ [L].

From the experimental point of view, the measurement of the functions $S(d)$ and $L(d)$ is inspired by Tirel et al. (2020). Performed on the two-gray level images, an Euclidian Distance Map image of the liquid system is built by assigning to each black pixel (representing a liquid pixel) a gray level value equal to its distance (in pixels) from the closest interface point. The cumulative count of the number of pixels as a function of the gray level allows to draw the cumulative scale distribution $E_2(d)$ defined as $E_2(d) = S(0) - S(d)$: $E_2(d)$ increases from 0 to $S(0)$ when d increases from 0 to d_M. The derivative of $E_2(d)$ with respect to the scale d is the scale distribution noted $e_2(d)$: $e_2(d) = E_2(d)_{,d}$. It can be shown that $e_2(d) = L(d)/2$. In the measuring procedure, each derivative step is preceded by a moving average of the function to be derived in order to attenuate the inaccuracy due to pixelisation. In the following, the notations *L*(*d*) and $e_2(d)$ are maintained and designate the theoretical and measured eroded system contour length, respectively.

As an illustration, the measuring technique is applied on the synthetic image shown in Fig. 3 that corresponds to a 200 pixels diameter column disturbed by a sinusoidal perturbation of wavelength $\lambda = 800$ pixels and amplitude $Ap = 20$ pixels. The image is one wavelength long ($n = 2$), the reach $d_R = 160$ pixels and the maximum scale $d_M = 240$ pixels (see Fig. 3). The cumulative scale distribution $E_2(d)$ measured on this image increases continuously from 0 to a maximum value (see Fig. 4). Reached at the scale d_M, this maximum value corresponds to the liquid system surface area. The measurement of d_M is based on the cumulative distribution: it is identified as the smallest scale for which $E_2(d) = S(0)$ (see Fig. 4).

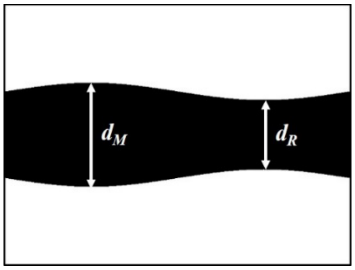

Figure 3: Synthetic image (600 pixels x 800 pixels). Unperturbed diameter $D = 2a = 200$ pixels, Distrubance wavelength $\lambda = 800$ pixels, Disturbance amplitude $Ap = 20$ pixels ($d_R = 160$ pixels, $d_M = 240$ pixels).

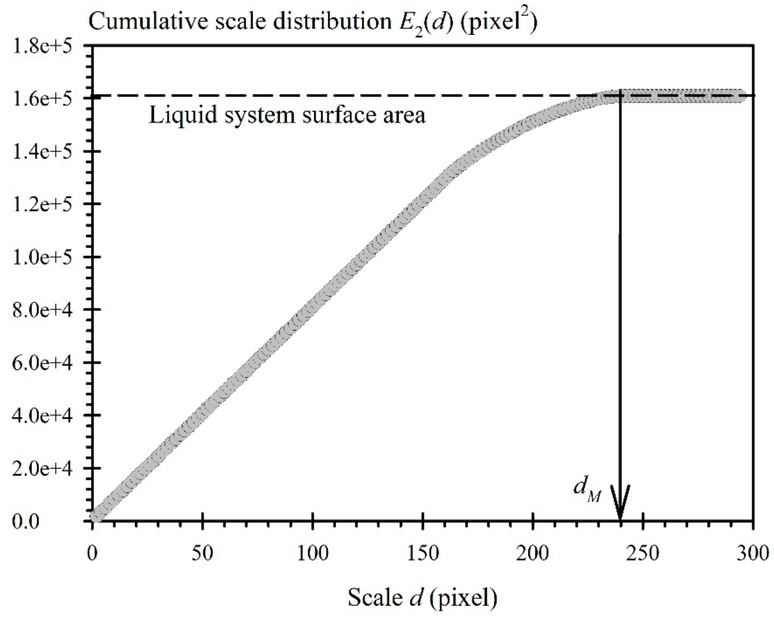

Figure 4: Cumulative scale distribution $E_2(d)$ measured on Fig. 3. Determination of the scale d_M.

The scale distribution $e_2(d)$ of the synthetic image is plotted in Fig. 5. For scales less that d_R, $e_2(d)$ is expected to be constant since all parallel systems have the same circumference as the liquid system. This behavior is obtained only on average. The distance to the interface assigned by the Euclidian Distance Map process to each liquid pixel always corresponds to an integer number of pixels. This introduces inaccuracies that are compensated for from one erosion to the next one, leading to the oscillations observed in Fig. 4. The abrupt change in slope of $e_2(d)$ at scale d_R has been used to establish the following protocol to determine this scale. Two requirements have to be fulfilled at d_R; (1) $0.95\ e_{2p} < e_2(d_R) < 1.05\ e_{2p}$ where e_{2p} is the plateau value of $e_2(d)$ in the small-scale region; (2) The difference $(e_2(d_R) - e_2(d_{R+1}))$ must have a minimum value adjusted to each situation (the scale d_{R+1} represents the scale following d_R in the discrete experimental scale series). The value of e_{2p} is determined as the average of $e_2(d)$ from the fourth to the tenth points. (These points are shown in black in Fig. 5.) Decreasing the scale from d_M, the scale d_R is the first one that fulfills these two requirements. If no solution is obtained, the second condition criteria is reduced and the whole protocol is applied again. As far as the measurement performed on Fig. 3 is concerned, Figs. 4 and 5 report the expected values: $d_M = 240$ pixels and $d_R = 160$ pixels. Thus, the corresponding perturbation amplitude obtained by $Ap = (d_M - d_R)/4$ is well determined also.

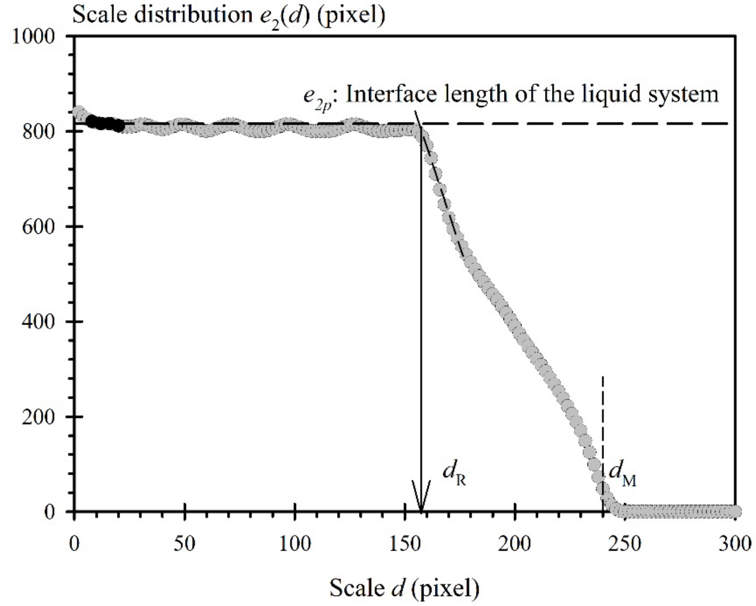

Figure 5: Scale distribution $e_2(d)$ obtained for Fig. 3. Black points are used to calculate the constant e_{2p}. Determination of the reach d_R (d_M is the maximum scale determined in Fig. 4)

Figure 6 shows as points, the derivative -$e_2(d)_{,d}$ determined by the above procedure from synthetic image data, the one shown in Fig. 3 (Ap = 20 [L]) as well as for another case with a smaller amplitude (Ap = 10 [L]). Also plotted on Fig. 6 as lines, are the analytical expectation -$L(d)_{,d}/2$ as derived in the appendix and also plotted in Fig. 2 for the same conditions. Considering that the smoothing operations in the numerical protocol exclude the detection of discontinuities, a rather satisfactory agreement is obtained between -$e_2(d)_{,d}$ and the analytical -$L(d)_{,d}/2$, at least in the region of interest between the scales d_R and d_M. This result validates the measurement procedure, which was then applied to experimental image data.

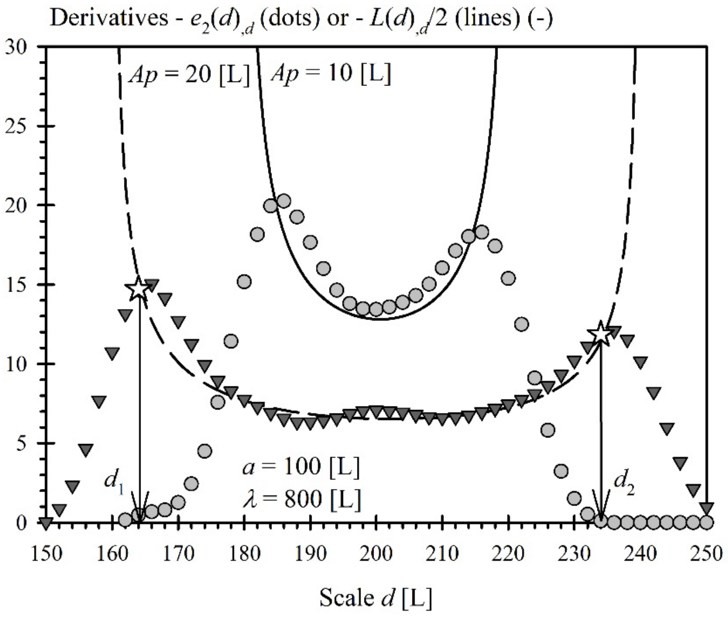

Figure 6: Derivative -$e_2(d)_{,d}$ (dots) and -$L(d)_{,d}$ (lines) for a cylindrical system (a = 100 [L]) sinusoidally perturbed (λ = 800 [L]): circles and solid line Ap = 10 [L], triangles and dashed line Ap = 20 [L]. Wavelengths are estimated at star dots (shown for Ap = 20 [L] only) corresponding to scales d_1 and d_2.

We note in Fig. 6 that the -$e_2(d)_{,d}$ point immediately before each maximum (star dots in Fig 6 for Ap = 20 [L]) fits well with the analytical value -$L(d)_{,d}/2$. For clarity, only the Ap = 10 [L] and 20 [L] are shown in Fig. 6 but this has been observed for numerous cases over a range of wavelength and amplitude. From the definition of -$L(d)_{,d}/2$ derived the appendix, the coordinates of each point together with the amplitude Ap of the disturbance allow the evaluation of a wavelength. The left point is associated with a scale d_1 (see Fig. 6 for $Ap = 20$ [L]) which is close to d_R (for $Ap = 20$ [L], $d_1 = 164$ [L] and $d_R = 160$ [L]). The wavelength λ_1 evaluated at this point must be seen as the wavelength of the sinusoid that best fits the system interface in the contraction region. Similarly, the right point is associated with the scale d_2 (see Fig. 6 for $Ap = 20$ [L]) which is close to d_M (when $Ap = 20$ [L], $d_2 = 234$ [L] and $d_M = 240$ [L]). The wavelength λ_2 evaluated at this point, must be seen as the wavelength of the sinusoid that best fits the system interface in the swelling region. If the perturbation of the system is purely sinusoidal, the wavelengths λ_1 and λ_2 are expected to be equal. This is satisfactorily obtained for the cases presented in Fig. 6: when $Ap = 20$ [L], $\lambda_1 = 825$ [L] and $\lambda_2 = 795$ [L] which is close to the wavelength of the perturbation (800 [L]). This result shows that the procedure to evaluate the local deformation wavelength is acceptable. Of course, if the deformation is not perfectly sinusoidal, λ_1 and λ_2 will have different values and this difference will inform on the nature of the system deformation. In particular, for a BOAS structure, we would expect to find a large wavelength λ_1, as the curvature in the image plane at the level of the ligaments is zero. Therefore, an increase of the λ_1/λ_2 ratio would indicate a jet deformation that evolves towards a BOAS structure.

Now applying the analyses described above to experimental images of the local jet sequences allows having at each position of the AW, distributions of scale distribution $e_2(d)$, scale d_R, maximum scale d_M, wavelengths λ_1 and λ_2. Averages noted $\langle \bullet \rangle$ are arithmetic means:

$$\langle \bullet \rangle = \frac{1}{N_t} \sum_{i=1}^{N_t} \bullet_i \tag{6}$$

where N_t is the total number of images on which the distribution has been built.

Figure 7 shows d_R and d_M distributions obtained for S8 ($We = 37$) at a position ($z = 22.4$ mm) where the jet is in the ECR and shows BOAS patterns. The d_R peak (left peak in Fig. 7) represents the distribution of the diameter of the ligaments of the BOAS seen at this position and the d_M peak (right peak in Fig. 7) represents the distribution of the bead diameters. Note a non-negligible population of small values of d_M (less than 300 μm in Fig. 7), which corresponds to images containing only part of a bead or none at all when the ligament is longer than the AW. The presence of long ligaments may result from the beads coalescence following their migration along the string. Counting the percentage of images without beads and following the spatial evolution of this count is a marker of the coalescence mechanism. This is how the coalescence mechanism will be evaluated in this work.

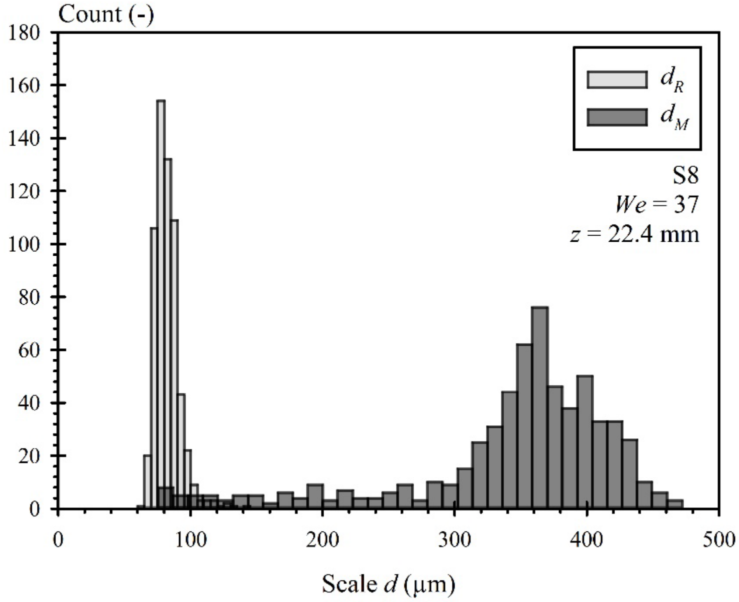

Figure 7: Example of d_R and d_M distributions. S8, $We = 37$, $z = 22.4$ mm. At this position, the jet is in the ECR.

4 - Results

4.1 - Regimes and characteristic distances

Similar to the analysis proposed by Christanti and Walker (2001), Fig. 8 maps the jet regimes for all operating conditions. The distances characterizing the regimes are divided by the nozzle orifice diameter, and the working conditions are identified by a Deborah number named De_{or} defined by: $De_{or} = t_{RZ}V_{or}/D_{or}$. Four regimes are distinguished: 1 – Neutral Regime (NR): [0; Z_{onset}], 2 – Inertio-Capillary Regime (ICR): [Z_{onset}; Z_{eci}], 3 – A mixed between ICR and the Elasto-Capillary Regime (ECR): [Z_{eci}; Z_{ecp}], 4 – ECR: [Z_{ecp}; Z_{ecf}], 5 – Final Regime (FR): [Z_{ecf}; L_{BU}]. The distances Z_{onset} and L_{BU} are determined according to the protocol presented in the previous section. The determination of distances Z_{eci}, Z_{ecp} and Z_{ecf} is explained below.

Figure 8 shows that S06 and S1 jets are shorter than for S5 and S8, and in the images, the typical viscoelastic jets regimes (ECR and FER) were not observed with these solutions. In contrast to the viscoelastic cases, the jets of S06 and S1 break up into drops very quickly after the initiation of the capillary instability. The rapid growth of the disturbance was associated with the final regime (FR) in Fig. 8. Similar to Newtonian liquid jets, this behavior suggests that the capillary instability of S06 and S1 jets is free of any observable viscoelastic effect. Conversely, the viscoelastic jet regimes are well identified for S5 and S8 jets and are responsible for the increase of the breakup length.

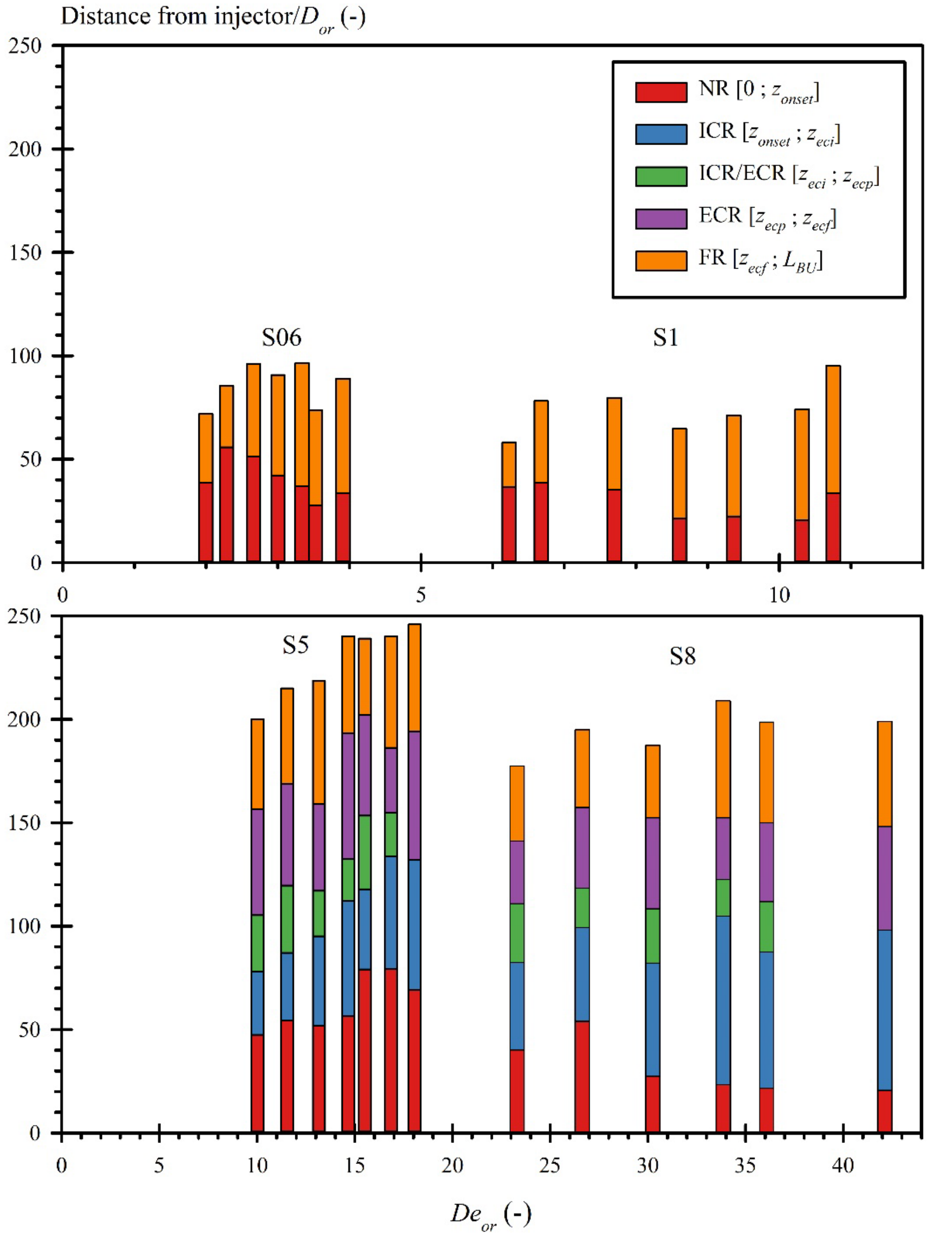

Figure 8: Regime maps of the jets.

All jets studied in this work have in common the existence of a neutral regime (NR). The length of this regime (Z_{onset}) depends on the flow rate: For S06, S1 and S8, the average behavior of Z_{onset} is to decrease when the flow rate increases, while the opposite behavior is observed for S5. As summarized in the introduction, the literature attributes the existence of this regime to the relaxation of the flow velocity profile, and, for viscoelastic jets, to the relaxation of a tensile stress. The establishment of the NR is therefore intimately linked to the injector internal flow development. In the present work, the orifice length is much smaller than the velocity profiling lengths (ranging from 8 to 17 mm for the studied jets). Therefore, velocity profile at the nozzle exit depends on the flow rate. As the flow rate increases, it is less developed at the injector outlet and its relaxation length decreases accordingly. This behavior corresponds to the one observed for the S06 and S1 jets, which showed a decreasing Z_{onset}. For these cases, attributing the length of the NR to the length of the velocity profile relaxation seems to explain the results. However, this conclusion does not hold for S5 jets for which Z_{onset} clearly increases as the jet velocity increases. For viscoelastic cases, the analysis must consider the presence and relaxation of tensile stress. This is discussed later in this paper.

During the NR, the jets show both azimuthal and stationary deformations (Tirel, 2019) for which they are expected to be stable according to the non-viscous jet linear theory (Rayleigh, 1878). Also, for the sinusoidal perturbation of the capillary instability to develop, the jet must have recovered a sufficiently cylindrical shape. Thus, we may consider that the jet has recovered a cylindrical shape in the Z_{onset} region. This position appears therefore ideal for determining the diameter D_j of the jet using the relation:

$$D_j = \left\langle \frac{d_R\left(Z_{onset}\right) + d_M\left(Z_{onset}\right)}{2} \right\rangle \tag{7}$$

D_j's average deviation from D_{or} is 5%, and never exceeds 7%. The contraction or expansion of the jets is therefore negligible, which confirms the absence of shear thinning effect.

As far as the other regimes are concerned, we note for S06 and S1 that the length of the FR increases with the flow rate recalling the behavior described by the linear theory (Rayleigh, 1878). This point will be clarified later on. For S5 and S8 jets, as the flow rate increases, the length of the

ICR increases while that of the mixed regime (ICR-ECR) decreases down to zero. The transition from ICR to ECR happens progressively quicker as the flow rate increases. Eventually the flow rate is sufficiently high that the transition occurs on a length scale shorter than the wavelength, so no mixed flow regime is observed. Finally, the ECR and FR show no significant length variation with the flow rate for both S5 and S8.

Using the results presented in Fig. 8, the dimensionless capillary instability length defined as $(L_{BU} - Z_{onset})/D_j$ is plotted as a function of the square root of We in Fig. 9. S06 and S1 jet instability lengths appear proportional to $(We)^{0.5}$ in accordance with the model of Grant and Middleman (1966) for instance insofar as the jets studied have a low viscosity ($3Oh \ll 1$). This is further indication that S06 and S1 jets are displaying solely a Newtonian response. However, the proportionality coefficient obtained here (3.72) is much lower than the 19.5 reported by Grant and Middleman (1966) probably because the jet instability length in Fig. 9 is the distance between the position at which the disturbance is detectable to the average breakup position.

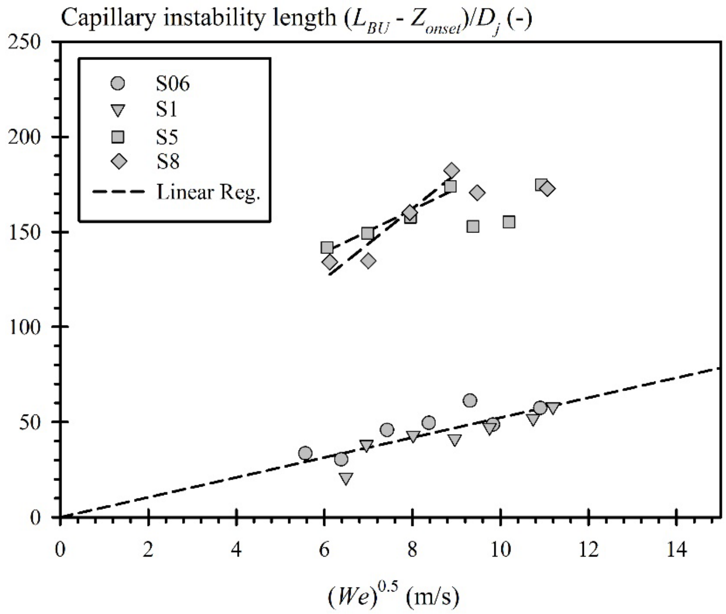

Figure 9: Capillary instability length $(L_{BU} - Z_{onset})/D_j$ as a function of the square root of the Weber number We.

S5 and S8 jets show much longer capillary instability lengths than the two other solution jets. First, the jet instability length increases linearly when $We^{0.5}$ increases for $We^{0.5} < \sim 9$ and then stops increasing to remain roughly constant for higher $We^{0.5}$. Surprisingly, despite the differences in their solution properties (see Tables 1 and 2), we note that S5 and S8 solution jets show similar capillary instability lengths. This suggests solution property changes as reported by the results presented below.

4.2 - Wavelength and scale evolutions

Figures 10 and 11 present temporal evolutions of the wavelengths $<\lambda_1>$ and $<\lambda_2>$. In Tirel et al. (2020) the equivalent time t was calculated from the axial position z, the jet velocity V_j (= $8Q_v/\pi D_j^2$) and the gravitational acceleration g. For the parameters of this study, V_j is always much greater than $2gz$, so the expression simplifies to $t = z/V_j$. In Figs. 10 and 11, the origin time is t_{onset} and the time is divided by the duration of the capillary instability, i.e., $t_{BU} - t_{onset}$, where the breakup time $t_{BU} = L_{BU}/V_j$. The measurements were performed at positions where the jet deformation is expected to be close to a sinusoid, i.e., in the FR for S06 and S1 and in ICR for S5 and S8. The wavelengths in Figs. 10 and 11 are divided by the jet diameter D_j. For inviscid jets, the Rayleigh linear theory evaluates this ratio at 4.51. It is indicated in the figures also.

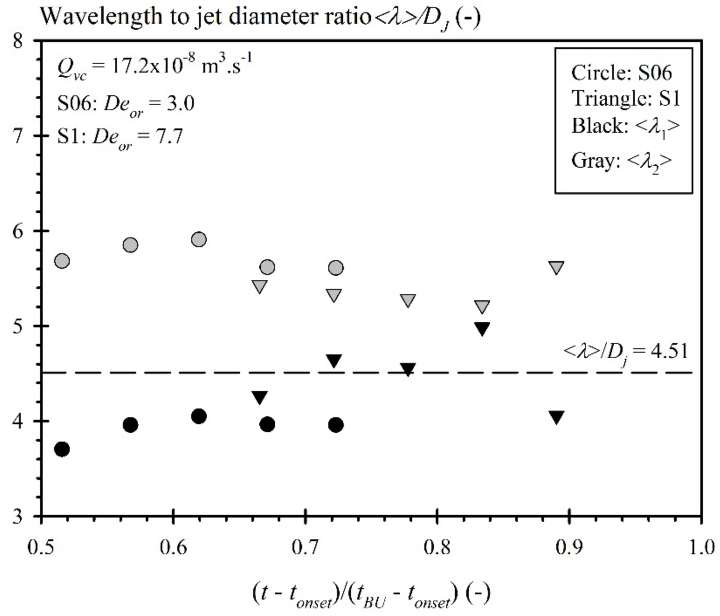

Figure 10: Temporal evolution of the wavelength ratios $<\lambda_1>/D_j$ and $< \lambda_2>/D_j$ (S06 and S1, $Q_{vc} = 17.2\text{x}10^{-8}$ m^3·s^{-1}).

Figure 10 shows results for S06 and S1 jets at $Q_{vc} = 17.2\text{x}10^{-8}$ m^3·s^{-1}. For both solutions and all flow rates, we observed that $<\lambda_1> \neq <\lambda_2>$. As explained above, this indicates that the jet deformation is never purely (single-mode) sinusoidal at the measurement locations. $<\lambda_1>$ and $<\lambda_2>$ remain rather parallel to each other over time for all S06 jets. The same behavior is observed for

S1jets except for the lowest flow rates for which <λ_1> and <λ_2> tend to get closer together with time illustrating a more and more sinusoidal disturbance.

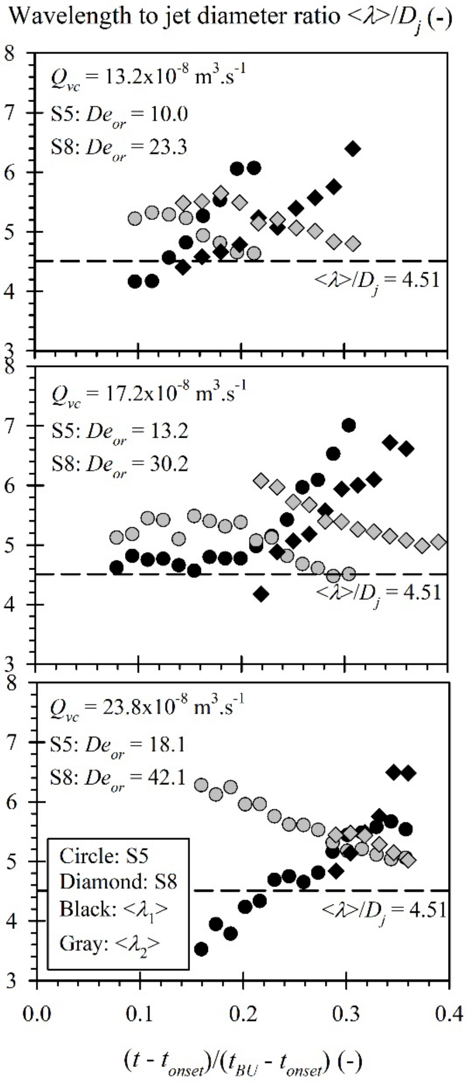

Figure 11: Temporal evolution of the wavelength <λ_1> and <λ_2> (S5 and S8, three Q_{vc}).

Figure 11 shows the results for S5 and S8 jets at three flow rates. As for the previous solutions, <λ_1> < <λ_2> at the earliest positions, revealing that the disturbance is not purely (single-mode) sinusoidal there. However, the wavelengths show a temporal evolution not observed for S06 and S1 jets, i.e., as time increases, <λ_1> increases while <λ_2> decreases. As explained in section 3.3, the significant increase of <λ_1> makes sense and can be interpreted as an evolution of the perturbation towards a BOAS pattern. Thus, the growth of <λ_1> illustrates the entry into action of viscoelastic effects in the development of capillary instability. On the other hand, the decay of $<\lambda_2>$ as time increases reflects the evolution of swellings along the jet to more spherical shapes. We note in Fig. 11 that the deformation dynamics expressed by the increase of $<\lambda_1>$ always occurs earlier in the process for S5 jets than for S8 jets. However, when the flow rate increases, this time lag decreases and the behaviors of S5 and S8 jets become identical for the highest flow rate (Q_{vc} = 23.8x10^{-8} $m^3 \cdot s^{-1}$).

Adopting the same time basis as in Figs. 10 and 11, Fig. 12 displays the temporal evolution of the average maximum scale, $<d_M>$, the arithmetic mean of the largest jet diameters seen in the analyzing window (AW) at a given position z (or instant t). Where the jet deformation is of the BOAS type, $<d_M>$ represents the average diameter of the beads. The results are plotted for all solutions at Q_{vc} = 15.2x10^{-8} $m^3 \cdot s^{-1}$. For each case, a time interval during which a linear increase appears is clearly seen. Given the ordinate scales used in Fig. 12, these increases illustrate an exponential growth of $<d_M>$ over time, agreeing with the linear theory of inviscid jets (Rayleigh, 1878). The linear increase extends over the dimensionless time interval [0.3: 0.9] for S06 and S1 jets, i.e., over almost the entire duration of the capillary instability, which is an additional mark of the Newtonian behavior of these solutions. Conversely, for S5 and S8, the linear increase is observed at the beginning of the capillary instability, i.e., over the time interval [0.1; 0.2]. The slope of these behaviors gives access to the growth rate of the jet dilations. The dimensionless growth rates are plotted as a function of *We* in the insert in Fig. 12 where the theoretical value of an inviscid jet submitted to the optimum wavelength disturbance (i.e., 0.343) is also shown. We obtain growth rates slightly less than the theoretical value. Similar results were obtained for PEO solution small-diameter jets by Charpentier et al. (2017). This result is consistent with the fact that the deformation identified on the jets is not the optimum sinusoidal disturbance (see Figs. 10 and 11). We observe also that the growth rates do not allow differentiating between the solutions. As said above, this is coherent with the fact that the elastic contribution of the polymers is not yet sufficient to affect the flow in the ECR.

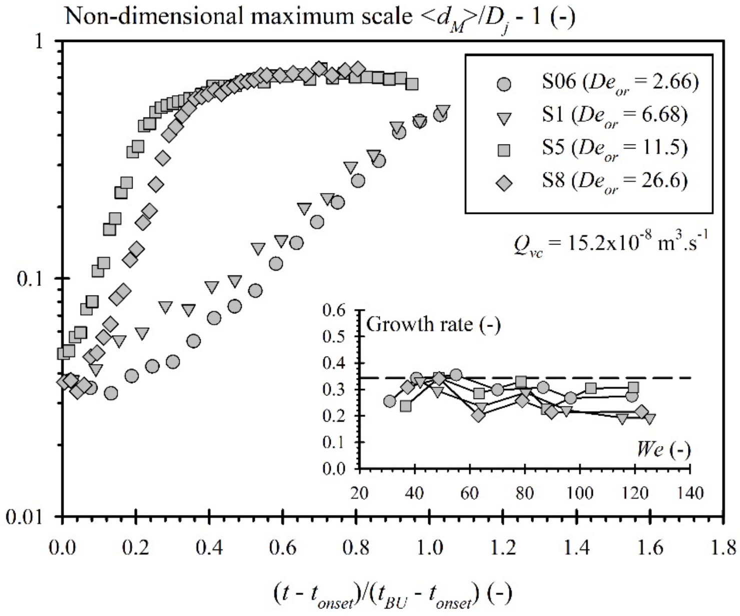

Figure 12: Temporal evolution of the mean maximum scale <d_M>
(All solutions, Q_{vc} = 15.2x10^{-8} m^3·s^{-1}).
Insert: dimensionless perturbation growth rate
(All working conditions, dashed line: theoretical value from non-viscous jet linear theory).

For the same operating conditions as in Fig. 12 and using the same temporal basis, Fig. 13 presents the temporal evolution of the arithmetic mean scale <d_R>, which is the average of the jet contraction diameters seen in the AW at a given location z or instant t. Where the jet deformation is of the BOAS type, <d_R> represents the average diameter of the ligaments between the beads. For each case, <d_R> decreases as the time increases which is reflected in the Fig. 13 by a continuous increase of (1 - <d_R>/D_j). For S06 and S1, these increases are similar and linear denoting a rather constant exponential decrease of <d_R> as reported by the inviscid jet linear theory (Rayleigh, 1878). For S5 and S8, (1 - <d_R>/D_j) shows two linear increases: the first corresponds to the exponential decrease of <d_R> during the ICR, and the second to the exponential decrease of <d_R> during the ECR. Drawing inspiration from Tirel et al. (2020), it is by analyzing the second dynamics that the extensional relaxation time and apparent and terminal elongational viscosities of the solutions are extracted. This is presented in the next sub-section.

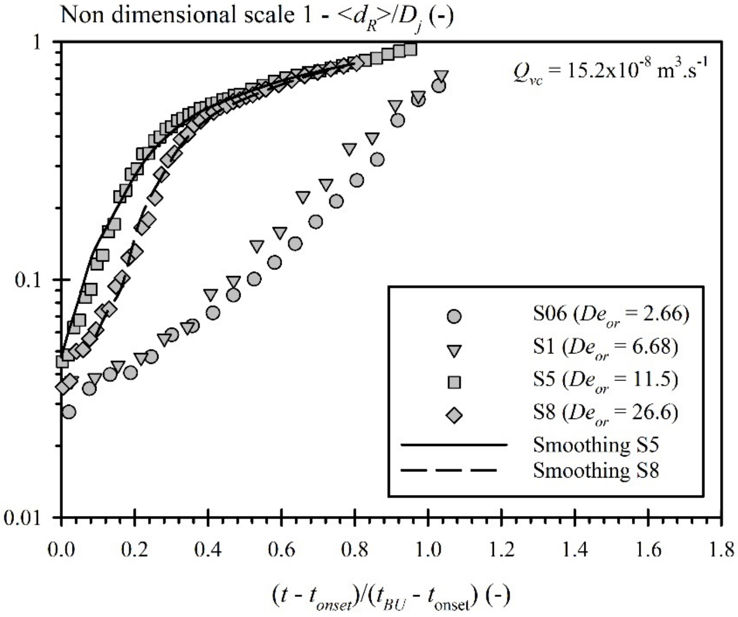

Figure 13: Temporal evolution of mean scale <d_R>
(All solutions, Q_{vc} = 15.2 10^{-8} m^3/s).

4.3 - Elasto-capillary regime: ECR

The temporal evolution of a ligament diameter during the ECR allows determination of the extensional relaxation time t_R and elongational viscosities, both apparent $\eta_{E,App}$ and terminal $\eta_{E,T}$. By assuming that all ligaments of BOAS pattern in the ECR have the same thinning dynamics, the extensional relaxation time and elongational viscosities can be obtained by analyzing the temporal evolution of a mean scale that has the same dynamics as the ligament thinning process (Tirel et al., 2020). In the present analysis, the average scale <d_R> is ideal since it is the arithmetic mean diameter of the ligaments. Thus, on the basis of this scale, an average flow deformation rate in the ligaments $\dot{\varepsilon}(t)$ is calculated:

$$\dot{\varepsilon}(t) = -\frac{2\langle d_R \rangle_{,t}}{\langle d_R \rangle} \tag{8}$$

as well as an average apparent elongational viscosity $\eta_{E,App}(t)$:

$$\eta_{E,App}(t) = -\frac{\sigma}{\langle d_R \rangle_{,t}} \quad (9)$$

Equations (8) and (9) involve the time derivative $<d_R>_{,t}$. To have a usable estimate of this derivative, it is recommended to smooth the temporal evolution of $<d_R>$ which is done by using the same smoothing tool as Tirel et al. (2020). An illustration of the quality of this smoother is shown in Fig. 13.

Figure 14 shows the temporal evolution of $1/\dot{\varepsilon}(t)$ and $\eta_{E,App}(t)$ for two different cases, one for S5 and one for S8, the present analysis being performed for these two solutions only. One way of identifying the ECR is to consider the evolution of $\eta_{E,App}(t)$, which increases over the course of this regime until it reaches a constant value. Figure 14 shows that this behavior is well observed. The time interval during which $\eta_{E,App}(t)$ is noted $[t_{eci}; t_{ecf}]$. During this time interval, we see in Fig. 14 that $1/\dot{\varepsilon}(t)$ is not constant: it increases from time t_{eci} to time t_{ecp} and then decreases from time t_{ecp} to time t_{ecf}. (Shown in Fig. 14, the times t_{eci}, t_{ecp} and t_{ecf} were used to calculate the positions Z_{eci}, Z_{ecp} and Z_{ecf} shown in Fig. 8.) It was observed that the time interval $[t_{eci}; t_{ecp}]$ actually corresponds to the mixed ICR-ECR regime and we decided to consider the ECR that extends in the time interval $[t_{ecp}; t_{ecf}]$.

In the ERC, the extensional relaxation time t_R is proportional to the inverse of this rate. Jetting experiments over a range of Weber number *We* from 1 to 80, which corresponds to their experimental setup limit, Mathues et al (2018) demonstrated that the time scale of the ligament diameter exponential decay in the ECR is $2t_R$ and thus, using Eq. (8), that $t_R = 1/\dot{\varepsilon}(t)$. Considering the Weber numbers of the present jets (see Table 2) we assume that this relation is appropriate for our cases. Thus, the increase of the deformation rate during the ECR suggests a continuous decrease of the extensional relaxation rate. In the following analysis, we consider two specific elongational relaxation times, i.e., t_{Ri} obtained at time t_{ecp} and t_{Rf} obtained at time t_{ecf} (see Fig. 14). These two elongational relaxation times are plotted in Fig. 15 for all S5 and S8 jets.

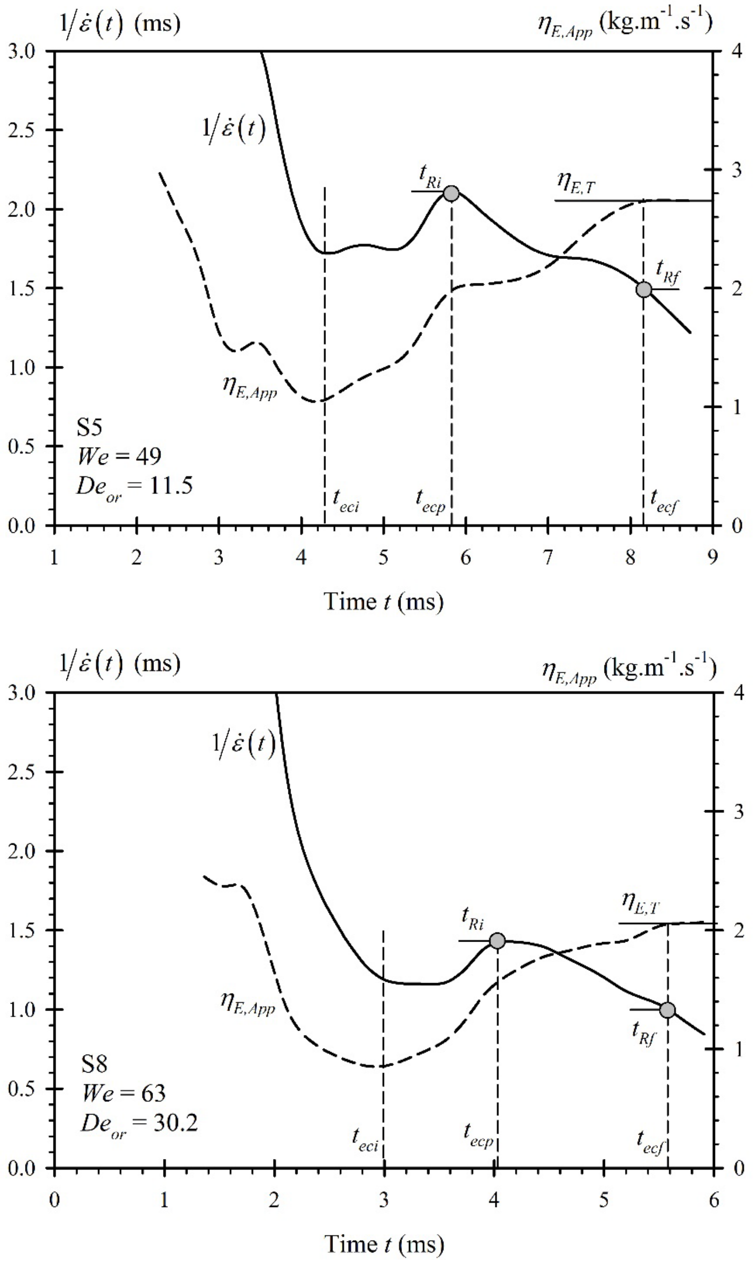

Figure 14: Temporal evolutions of inverse of the deformation rate $1/\dot{\varepsilon}(t)$ and of apparent viscosity $\eta_{E,App}(t)$.
Introduction of t_{eci}, t_{ecp}, t_{ecf}, t_{Ri}, t_{Rf}, $\eta_{E,T}$
(Top: S5, $Q_{vc} = 15.2\ 10^{-8}$ m^3/s, Bottom: S8, $Q_{vc} = 17.2\ 10^{-8}$ m^3/s).

4.3.1 - The extensional relaxation time t_{Ri}

Extensional relaxation time is a material property of the polymer, a function of the molar mass and concentration: it is expected to be independent of flow rate. However, for both solutions, Fig. 15 shows a decrease of the extensional relaxation time t_{Ri} as the Weber number increases. Reported by other works (Tirel et al. 2020, Brenn and Stelter 2020) this behavior denotes polymer degradation mechanism in the injector. This can be demonstrated by considering Merrill and Leopairat's investigation (1980) in which the molar weights of polymers were measured before and after having been degraded by an extensional flow. The effect of degradation was associated with a scission index SI_{inj} defined as the number of additional polymer molecules created per initial polymer molecule, namely:

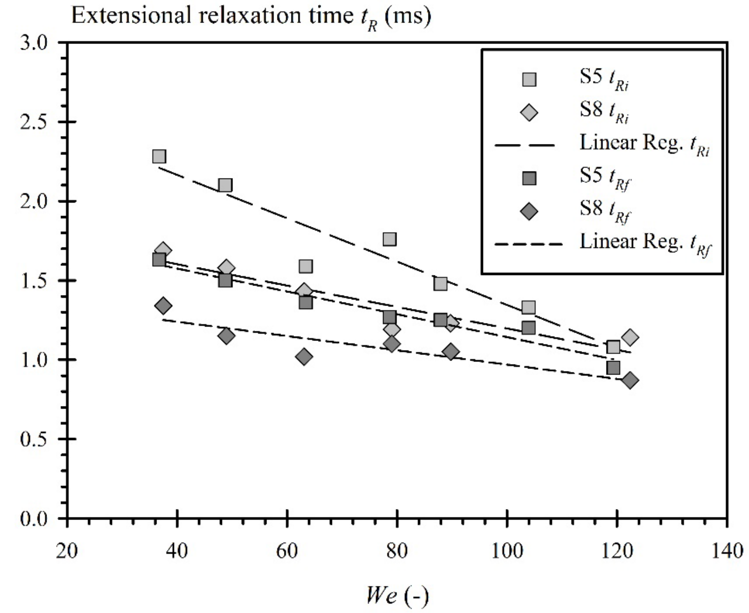

Figure 15: Evolution of extensional relaxation times t_{Ri} and t_{Rf} versus the Weber number We. (S5 and S8).

$$SI_{inj} = \frac{\bar{M}_{n,0}}{\bar{M}_n} - 1 \tag{10}$$

where $\bar{M}_n$ is the number average molar weight and $\bar{M}_{n,0}$ is the initial value thereof. Their experimental results revealed the following correlation:

$$\frac{\mathrm{d}SI_{inj}}{\mathrm{d}V_{inj}} \propto \left(\bar{M}_{n,0}\right)^{\alpha} \tag{11}$$

with $\alpha = 2.23$. Combining Eqs. (1) and (10) allows expressing the scission index as a function of the extensional relaxation time:

$$SI_{inj} = \left(\frac{t_{R0}}{t_R} \right)^{1/3\upsilon} - 1 \quad (12)$$

where t_{R0} is the extensional relaxation time of the fresh solution. Introducing $t_R = t_{Ri}$ and $t_{R0} = t_{RZ}$ in Eq. (12) gives an estimation of the scission index due to injection in the experiment. Presented in Fig. 16, the results show scission indexes that increase linearly as the flow velocity increases, agreeing will Merrill and Leopairat (1980) (see Eq. (11)). Therefore, the dependence of the extensional relaxation time t_{Ri} on the flow rate observed here is due to polymer degradation in the injector. The slope of the linear evolution of SI_{inj} is slightly greater for S8 than for S5, but both are much smaller than that obtained by Merrill and Leopairat (1980) (α in Eq. (11) is of the order of 0.33 here). This difference may be attributed to different experimental conditions and to the way scission indices are estimated. Figure 16 also shows that scission indexes are higher for S8 than for S5, which is a manifestation of the smaller relaxation time t_{Ri} for this solution. The results indicate that the polymers for S8 undergo 2 to 3 splits as according to the flow rate while this number drops to 0.5 to 1 for S5. This expresses the importance of the polymer molar mass with respect to polymer degradation upon injection.

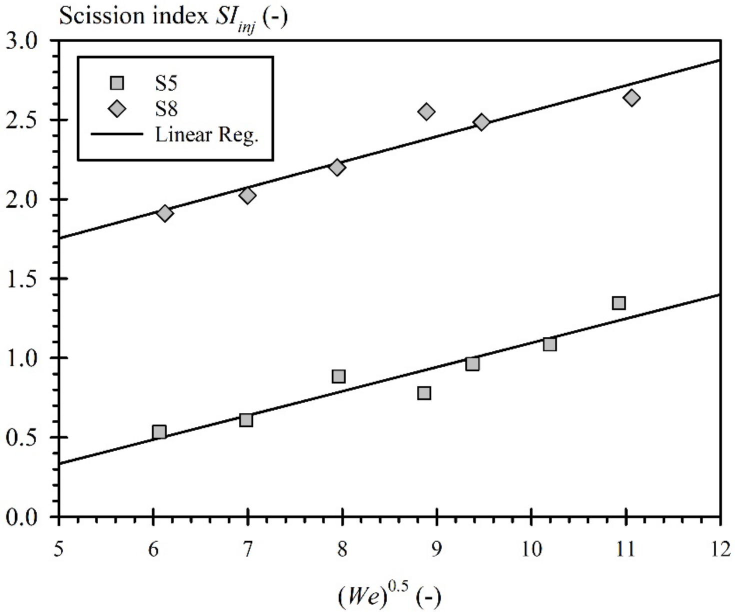

Figure 16: Injection scission index versus the square root of the Weber number *We* (S5 and S8).

Note in Fig. 15 that at the highest flow rate, the same extensional relaxation time t_{Ri} is obtained for solutions S5 and S8. As shown in Fig. 11-bottom, this flow rate is the one for which the deformation of S5 and S8 jets occur at the same time.

Experimental investigations due to Stelter et al. (2002b) and Brenn and Stelter (2020) on the injection of viscoelastic solutions established a correlation between the mechanical degradation of polymer in the injector represented by the ratio of the extensional relaxation time of the degraded to the fresh solution (t_R/t_{R0}) and a Deborah number involving injector internal dimension. For jets of PEO solutions, Brenn and Stelter (2020) reported:

$$\frac{t_R}{t_{R0}} = 1.3819 De_{BS}{}^{-0.5146} \tag{13}$$

with $De_{BS} = t_{R0}(V_{or}/D_{in})$ the Deborah number and D_{in} the entrance diameter of the nozzle. By taking $t_{R0} = t_{RZ}$ and $t_R = t_{Ri}$, and the value of D_{in} given in section 2.1, we see in Fig. 17 that the mechanical degradation observed here depends on the Deborah number $De_{or}(D_{or}/D_{in})$ in a similar way as found by Brenn and Stelter (2020). The coefficients of the dependence are different, probably due to the very different operating conditions between the two studies.

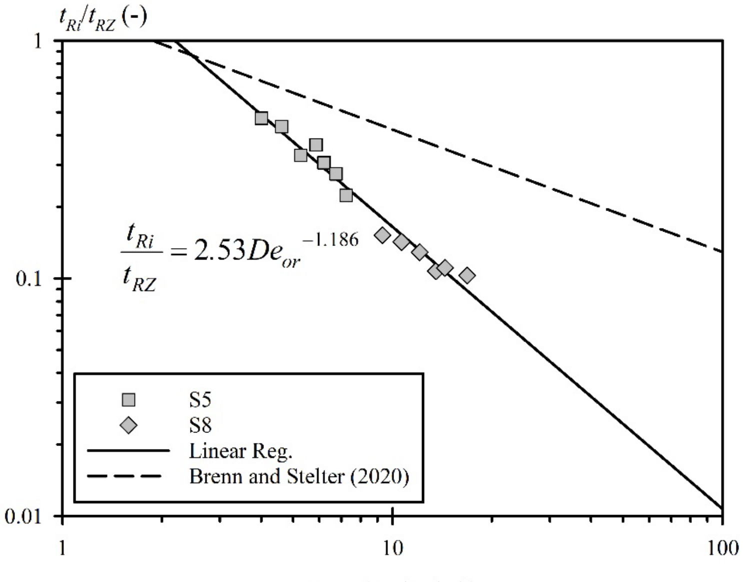

Figure 17: Ratio of extensional relaxation time of degraded and fresh solution as a function of the Deborah number of the nozzle flow. Comparison with Brenn and Stelter (2020) (S5 and S8).

In addition to a higher scission indexes, the smaller relaxation times t_{Ri} obtained for S8 compared to S5 reveal also that S8 jets are less axially tensed at the nozzle exit than S5 jets. At this point, it is worth asking whether the early onset of capillary instability observed for S8 jets at high flow rates (see Fig. 8) is related to an early relaxation of the axial tension. To evaluate this point, the works of Goren and Gottlieb (1982) and Bousfield et al. (1986) are considered. According to Goren and Gottlieb (1982), the decrease of the axial tension with the distance from the nozzle expresses as:

$$Te(z) = T_0 \exp\left(-\frac{z}{t_R V_j}\right) \tag{14}$$

Furthermore, Bousfield et al. (1986) expressed the initial axial tension T_0. Being made dimensionless by the tension $2\sigma/D_j$, the initial axial tension expresses:

$$T_0 = \frac{32}{3}\frac{\left(1-\frac{t_D}{t_R}\right)\mu_L D_j}{2t_R\sigma}\left(\frac{2t_R V_j}{D_j}\right)^2 \tag{15}$$

where the retardation time t_D can be estimated by $(\mu_s/\mu_L)t_R$. Combining these equations leads to:

$$Te(z) = \frac{64}{3}\frac{(\mu_L-\mu_s)t_R V_j^2}{D_j\sigma}\exp\left(-\frac{z}{t_R V_j}\right) \tag{16}$$

The axial tension at the Z_{onset} position, estimated with Eq. (16) by taking $t_R = t_{Ri}$, are plotted in Fig. 18. We note that the axial tensions at Z_{onset} range from 1 to 2 and are rather independent of the flow rate for S5 jets. Thus, for this solution, the onset of capillary instability occurs when the axial tension has decreased to a value of the order of the constant capillary tension. Associating the appearance of capillary instability with the axial tension relaxation is therefore appropriate here.

This also seems to be the case for the S8 jets at the two smallest flow rates for which the $T_e(Z_{onset})$ are of the same order of magnitude as those of the S5 jets. However, this scenario no longer holds for higher flow rates for which the axial tension at Z_{onset} is much larger and shows a rather linear increase as the flow rate increases. We infer from these results that the early triggers of capillary instability observed at high flow rates for S8 jets is not related to the relaxation of axial tension. This result also shows that capillary instability can be triggered even if the axial tension is not relaxed.

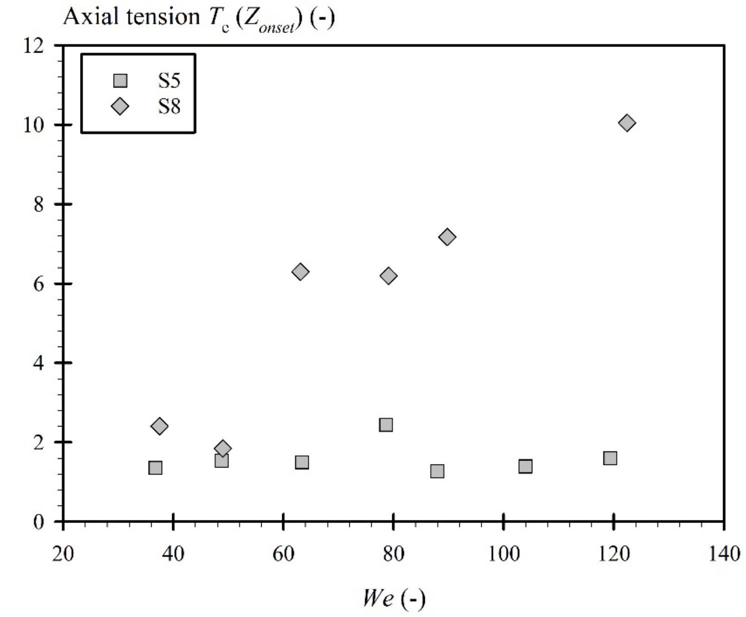

Figure 18: Axial tension at position Z_{onset} versus Weber number We (S5 and S8 jets).

4.3.2 - The extensional relaxation time t_{Rf}

The relaxation times t_{Rf} defined in Fig. 14 and shown in Fig. 15 as a function of the Weber number always report smaller values than t_{Ri}. This behavior suggests the presence of further polymer mechanical degradation during ECR. As said in the introduction, the presence of this mechanism in atomization processes has been evoked in the literature (Yarin 1993; Stelter et al. 2000, Gaillard et al. 2022) because of the high deformation rates involved. In this work, these rates are of the order of 0.5 10^3 to 10^3 s^{-1} (see Fig. 14). By positing $t_{R0} = t_{Ri}$ and $t_R = t_{Rf}$ in Eq. (12), the scission index during the ECR, SI_{ECR}, is estimated. Figure 19 shows that SI_{ECR} are much lower than SI_{inj} and that their evolution is less obvious: on average, SI_{ECR} seems to decrease as the flow rate increases. However, as shown in the insert in Fig. 19, SI_{ECR} shows some correlation with the duration of the ECR (= $t_{ecf} - t_{ecp}$): SI_{ECR} increases with the regime duration when it is less than 1.7 to 2 ms according to the solution and saturates at 0.2 beyond this limit. Note that the time duration limits above which SI_{ECR} remain constant are of the order of the solution relaxation times (see Fig. 15). The correlation evidenced in the insert in Fig. 19 further supports the hypothesis that polymer degradation occurs during the ECR.

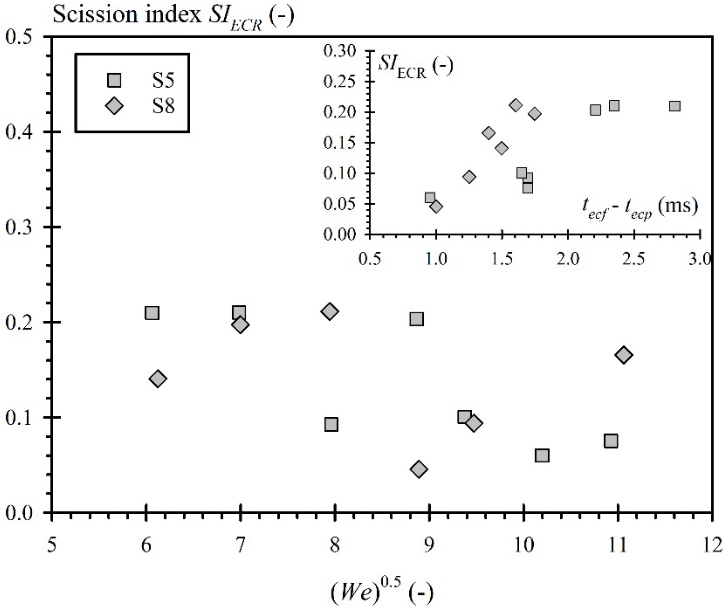

Figure 19: ERC scission index as a function of square root of the Weber number (S5 and S8) (Insert: SI_{ECR} versus ECR duration = $t_{ecf} - t_{ecp}$).

According to this last result, the relaxation time finds its final value after two sequences of polymer degradation (one in the injector, the second one during the ECR). Another element to evaluate the representativeness of this result is to verify the existence of a correlation between the terminal elongational viscosity and the final extensional relaxation time and to compare it with the results of the literature. To that end, we consider the terminal elongational viscosity $\eta_{E,T}$ and the extensional relaxation time t_{Rf}, which are the two solution characteristics at $t = t_{ecf}$ (see Fig. 14). Figure 20 reports a strong correlation between t_{Rf} and $\eta_{E,T}$ that is close to those expressed by the two models established by Stelter et al. (2002a, 2002b), one for flexible and one for rigid polymers. The present results are framed by the two models. It is worth mentioning that those models were established for very different operating conditions than those of the present study. The observed correlation participates in the validation of the experimental and analytical results of this work.

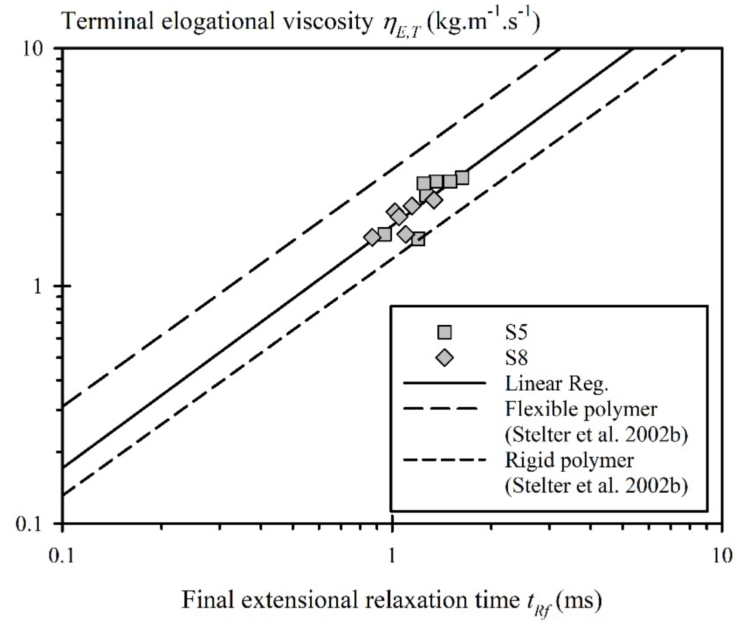

Figure 20: The terminal elongational viscosity $\eta_{E,T}$ as a function of the final extensional relaxation time t_{Rf}. (Stelter et al's (2002b) correlations – Flexible polymer: $\eta_{E,T}$ [kg.m^{-1}.s^{-1}]= 3074.9t_R [s] + 0.003 – Rigid polymer: $\eta_{E,T}$ [kg.m^{-1}.s^{-1}]= 1288.1t_R [s] + 0.003).

4.4 - Coalescence mechanism and spray mean drop diameter

Coalescence may be observed during the ECR and FER: a bead slides downstream or upstream along the ligament structure until it meets another bead and coalesces with it. In addition to increasing the size of the beads, the coalescence increases the length of the adjacent ligamentous portions of the BOAS structure and it is by considering this aspect that the intensity of this mechanism is quantified. At each position in the ECR and FER, the images of the local jet sequence showing a ligament only with no beads ($d_M \approx d_R$) are counted. In case of bead coalescence mechanism, this count grows with the time. Figure 21 plots the temporal evolution of this count during the ECR and FER for S5 and S8 jets at $We = 37$. The constant increase of the count illustrates that bead coalescence mechanism is effective during both the ECR and FER at an equivalent rate. We note however that the S8 jet reports a higher level of coalescence compared to the S5 jet. Figure 22 shows that this is observed for almost all flow rates. The reason for this is not identified in this work.

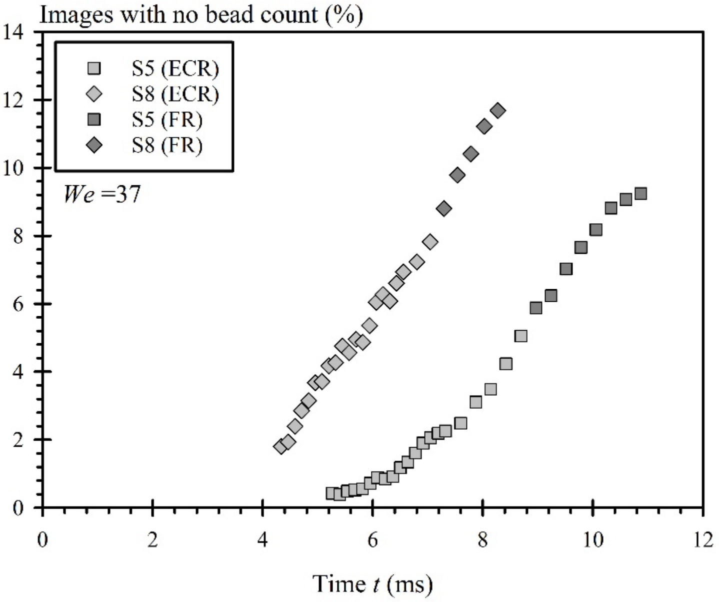

Figure 21: Coalescence mechanism evaluation as a function of time t (S5 and S8, *We* = 37)
(Count = percentage of local image with $d_M \approx d_R$)

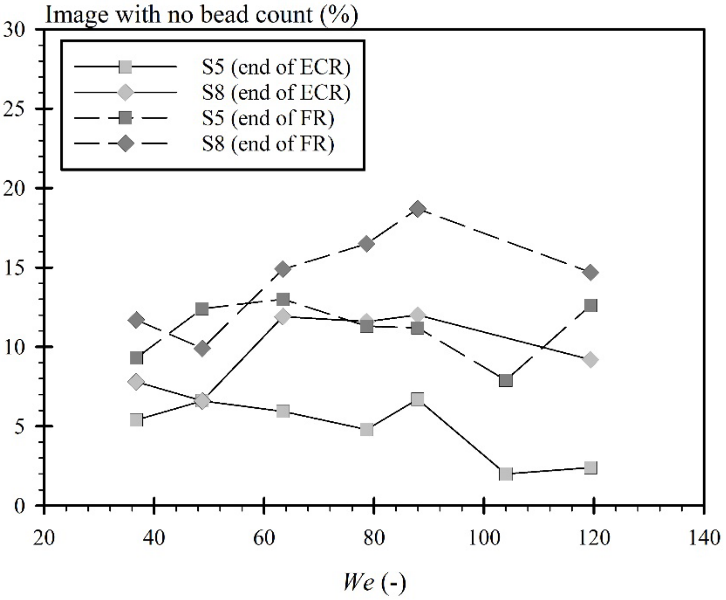

Figure 22: Coalescence mechanism evaluation at the end of ECR and FR as a function of the Weber number *We*.
(Count = percentage of local image with $d_M \approx d_R$)

If, as indicated by Li and Fontelos (2003), the migration and coalescence of beads on the BOAS structure does not influence the dynamics of ligament contraction, on the other hand, it must have an impact on the size of the drop produced. The drop diameter distributions are obtained from the scale distribution measured in the spray. Indeed, it was shown that, for a set of discs, the second derivative $e_2(d)_{,d,d}$ is proportional to the disc diameter distribution (Thiesset et al, 2019). By measuring the scale distribution beyond the breaking point, the drop diameter distributions are obtained and the arithmetic mean drop diameter D_{10} is calculated. For all operating conditions, Fig. 23 plots the D_{10}/D_j ratio versus the Weber number. Combining Rayleigh theory with a breakup pattern producing one drop per wavelength, a theoretical D_{10}/D_j ratio can be estimated to 1.89 for inviscid liquid jets. This value is plotted in Fig. 23. Two distinct behaviors appear. S06 and S1 sprays report very similar D_{10}/D_j ratios not depending on We and whose average value is 1.73. As shown in Fig. 10, the average wavelength of the capillary instability on these jets is larger than the theoretical optimum wavelength, which is favorable for the production of satellite drops and, consequently, of smaller big drops. On the other hand, S5 and S8 sprays show higher D_{10}/D_j ratios than the previous solutions and a certain variation of this ratio as We increases is observed, in particular for S8 sprays. These two observations show the influence of the coalescence mechanism on the drop diameter distribution. Indeed, as shown in Fig. 24, the average diameter of the drops correlates with the coalescence mechanism indicator found at the end of the FER in a very clear way.

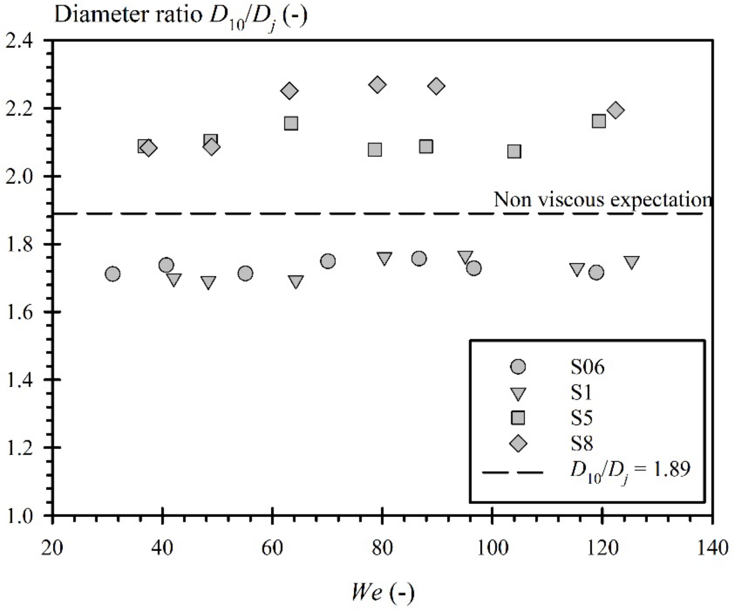

Figure 23: Diameter ratio D_{10}/D_j versus the Weber number We.

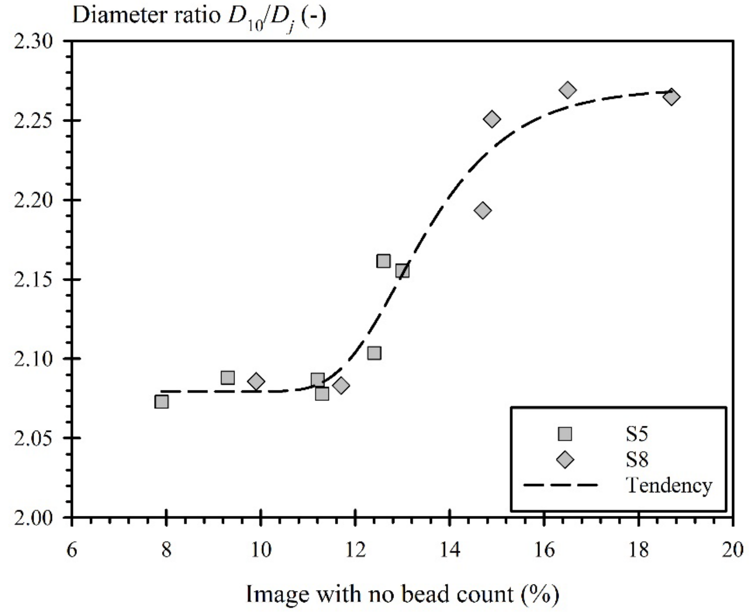

Figure 24: Diameter ration D_{10}/D_j versus image with no bead count (S5 and S8).

5 - Conclusion

One of the novel aspects of this experimental work is the development of analysis tools adapted to local and statistical studies of free jets of dilute polymer solutions. They are the POD of the local image series to identify the distance at which the capillary instability starts, the determination of local ruptures to obtain an average breakup length, and multi-scale description of the local jet shape to determine the initial deformation growth rate, the jet deformation dynamic, the local solution extensional relaxation time, the terminal elongational viscosity, the coalescence mechanism and the drop size distribution. The viscoelastic solutions contained the same polymer mass fraction (5 ppm) but with four different polymer molar masses and the jet velocity was maintained low enough so that the aerodynamic forces had no effect on the jet behavior.

The jets of the polymer solutions with the two lowest molar masses (0.6 and $1x10^3$ kg·mol^{-1}) reported no viscoelastic effect: no Bead On A String (BOAS) structures were observed and all quantified jet properties (neutral region length, instability duration, deformation wavelength and growth rate, drop size) match the Newtonian fluid expectations. This work does not say whether this non-detected viscoelastic effect is the consequence of polymer degradation in the injector.

Jets involving the higher molar mass polymers (5 and $8x10^3$ kg·mol$^{-1,}$ referred as S5 and S8) reveal viscoelastic effects at all tested velocities and two episodes of polymer mechanical degradation during the process were identified. The first episode occurs during the injection where the polymer degradation was proven by the evaluation of the scission index thanks to literature models. Moreover, scission indices 2.5 times greater for S8 than for S5 were obtained. This proportion is such that, after this degradation episode, the solution with the highest initial relaxation time ends up with the lowest extensional relaxation time. It is observed that this difference in extensional relaxation time has an effect on the development of the BOAS pattern that occurs earlier for S5 than for S8. The origin of the S8 jet over-degradation is not identified in this work.

The second degradation episode occurs during the ECR. Several elements support this scenario. First, the extensional relaxation time at the end of ECR is always smaller than the one measured at the beginning of this regime. Second, the scission indices related to this degradation episode, which are far less than those of the first one, correlate significantly with the duration of the regime. Third, the identified final relaxation times correlate with the terminal elongational viscosities in agreement with literature models, giving weight to the results and their interpretation.

Beside the over-degradation at the injection for S8 jets, other differences were noted between S5 and S8 jets. The length of the neutral regime increases continuously as the velocity increases for S5 jets, while it decreases for S8 jets. This difference cannot be explained by considering the axial tension undergone by the jets. On this question, we show that at the end of the neutral regime, the axial tension is always of the order of the surface tension contribution for S5 jets whereas it is much higher for S8 jets. Therefore, capillary instability can be triggered even if the axial tension undergone by the jet is little relaxed. In this case, another mechanism imposes perturbations on the jet with sufficiently strong amplitudes at the outlet of the injector to trigger the instability early on.

The last result concerns the bead coalescence mechanism that is found more frequent for S8 jets than for S5 Jets. The work does not say whether this difference is related to the over-degradation of S8 jets during injection. However, a clear correlation between the coalescence mechanism and the spray drop size is established.

These results demonstrate the richness of the approach adopted in this work, which consists in carrying out a fine and local analysis of the jets. While only average results have been presented in this article, each of them results from a distribution that is available. The diversity of the results is a credit to the multi-scale analysis which, by providing a complete description of the flow shape, is able to produce a wealth of information yet to be completed.

Appendix: The multi-scale description of deformed cylindrical liquid columns in air

The multi-scale description tool is applied to a sinusoidal deformed cylindrical liquid column in air as schematized in Fig. A.1 where half of the column is represented only with (0; z) being the axis of symmetry. The deformation wavelength is λ, the thick black line represents the liquid-gas interface and the grey lines represent three parallel systems obtained for three different erosion operation performed at scales d_1, d_2 and d_3 ($d_1 < d_2 < d_3$). A characteristic scale of the system is that for which the erosion operation erases the system completely. This maximum scale, denoted d_M, is shown in Fig. A.1: in this particular case, it corresponds to the diameter of the system at the largest jet cross-section. Furthermore, the reach of the system is the pinch-off diameter d_{po}.

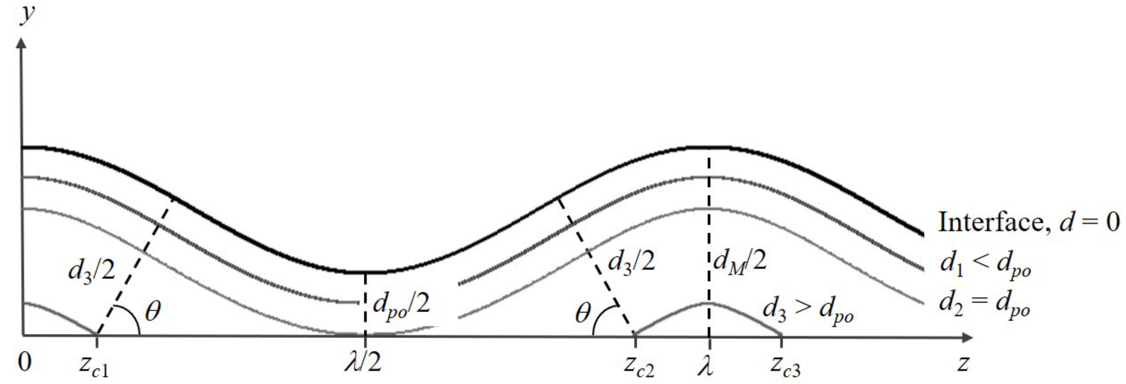

Figure A.1: Cylindrical liquid column submitted to a sinusoidal perturbation of wavelength λ (Half of the column is represented, (0; z) is the axis of symmetry)

In Dumouchel et al. (2022), it is demonstrated that:

For $d < d_{po}$ (d_1 in Fig. A.1 for instance):

$$\begin{cases} L(d) = -2S(d)_{,d} \\ H(d) = -2L(d)_{,d} \end{cases} \tag{A.1}$$

For $d \geq d_{po}$ (d_2 and d_3 in Fig. A.1 for instance):

$$\begin{cases} L(d) = -2S(d)_{,d} \\ H(d) + \sum_{i=1}^{n} C_i(\theta_i) = -2L(d)_{,d} \end{cases} \tag{A.2}$$

In Eq. (A2), n is the number of cusps and θ_i is the angle between the normal of the interface point that creates the i^{th} cusp and the (0; z) axis (see Fig. A.1). In the present case, the correction function $C_i(\theta_i)$ in Eq. (A.2) is (see Dumouchel et al. 2022):

$$C_i(\theta_i) = \tan(\theta_i) - \theta_i \tag{A.3}$$

The symmetry of the system leads to three important remarks. First, each correction function $C_i(\theta_i)$ has to be counted twice, i.e., for the upper and lower part of the ligament. Second, for any scale greater than or equal to the reach, the number of cusps n remains constant. Third, θ_i and $C_i(\theta_i)$ depend only on the erosion scale d and can be denoted $\theta(d)$ and $C(\theta(d))$ respectively. Furthermore, in 2D, H carries the role of the Euler characteristic χ, i.e., $H = 2\pi\chi$, with χ being equal to 0 or 1 if the system is homeomorphic to a 2D cylinder or to a disk, respectively. Therefore, we observe that if the eroded system is homeomorphic to one disk then the number of cusps is $n = 2$ and $H(d) = 2\pi$. This observation is generalized by writing: $H(d) = n\pi$. Including these elements as well as Eq. (A.3) in the second relation of Eq. (A.2) yields:

$$-2L(d)_{,d} = n\pi + 2n\big(\tan(\theta(d)) - \theta(d)\big) \tag{A.4}$$

For the system shown in Fig. A.1, a parametric expression of the function $L(d)_{,d}$ can be established by expressing the cusp coordinates as a function of those of the point on the interface creating this cusp. To do this, the interface is represented by $y = a + Ap\cos(kz)$ where a is the radius of the unperturbed column, Ap is the amplitude of the perturbation and $k = 2\pi/\lambda$ is the wavenumber. (The condition $Ap < \sqrt{\frac{a^2}{4} + \left(\frac{\lambda}{2\pi}\right)^2} - \frac{a}{2}$ is imposed to ensure that all cusps lie on the symmetric axis). This approach yields to the following parametric expression for $L(d)_{,d}$.

$$\begin{cases} d = 2\left(a + Ap\,cos\left(kz\right)\right)\sqrt{1+\left(K\,sin\left(kz\right)\right)^2} \\ -2L\left(d\right)_{,d} = n\pi + 2n\left(\dfrac{1}{K\,sin\left(kz\right)} - arctg\left(\dfrac{1}{K\,sin\left(kz\right)}\right)\right) \end{cases} \tag{A.6}$$

where $K = 2\pi Ap/\lambda$.

References

Blaisot JB, Adeline S. (2003) Instabilities on a free falling jet under an internal flow breakup mode regime. IJMF 29, 629-653

Bousfield DW, Keunings R, Marrucci G, Denn MM (1986) Nonlinear analysis of the surface tension driven breakup of viscoelastic filaments. J. Non-Newtonian Fluid Mech., 21:79-97

Brenn G, Stelter M (2020) A generalized Ohnesorge nomogram for liquid jet breakup regimes. Atom. And Sprays 30:213-238

Charpentier JB, Renoult MC, Crumeyrolle O, Mutabazi I (2017) Growth rate measurement in free jet experiments. Exp. Fluids 58:89

Christanti Y, Walker LM (2002) Effect of fluid relaxation time of dilute polymer solutions on jet breakup due to a forced disturbance. J Rheol 46(3):733–748

Cotton JP (1980) Polymer excluded volume exponent ν: An experimental verification of the n vector model for $n = 0$. J. Physique Lettres 41:L231-L234

Culter JD, Zakin JL, Patterson GK (1975) Mechanical degradation of dilute solutions of high polymers in capillary tube flow. Journal of Applied Polymer Science 19:3235-3240

Doi M, Edwards SF (1988) The theory of polymer dynamics. Clarendon Press – Oxford University Press

Dumouchel C, Thiesset F, Ménard T (2022) Morphology of contorted fluid structures. Int. Journal of Multiphase Flows 152:104055

Entov VM (1988) Elastic effects in flows of dilute polymer solutions. Progress and Trends in Rheology II, 260-262

Entov VM, Yarin AL (1984) Influence of elastic stresses on the capillary breakup of jets of dilute polymer solutions. Fluid Dyn. 19(1):21–29

Gaillard A, Sijs R, Bonn D. (2022) What determines the drop size in sprays of polymer solution? J. Non-Newtonian Fluid Mech. 305:104813

Gavis J, Gill SJ (1956) Tensile stress in jets of Viscoelastic fluids II. Journ. Of Polymer Science, XXI:353-362

Gavis J, Middleman S (1963) Origins of normal stress in capillary jets of Newtonian and Viscoelastic liquids. Journal of Applied Polymer Science, 7, 493-506

Gill SJ, Gavis J (1956) Tensile stress in jets of Viscoelastic fluids II. Journ. Of Polymer Science, XX:287-298

Grant RP, Middleman S (1966) Newtonian Jet Stability. AIChE Journal 12, n°4: 669-678

Goren SL, Gottlieb M (1982) Surface-tension –driven breakup of viscoelastic liquid threads. J. Fluid Mech. 120:245-266

Haward SJ, Odell JA, Li Z, Yuan XF (2010) Extensional rheology of dilute polymer solutions in oscillatory cross-slot flow: the transient behaviour of birefringent strands. Rheol Acta 49:633-345

James DF, Saringer JH (1982) Flow of dilute polymer solutions through converging channels. J. Non-Newtonian Fluid Mech. 35:421–443

Keshavarz B, Sharma V, Houze EC, Koerner MR, Moore JR, Cotts PM, Threlfall-Holmes P, McKinley GH (2015) Studying the effects of elongational properties on atomization of weakly viscoelastic solutions using Rayleigh Ohnesorge Jetting Extensional Rheometry (ROJER). J. Non-Newtonian Fluid Mech. 222:171–189

Larson RG (1999) The structure and rheology of complex fluids. Oxford University Press

Leib SJ, Goldstein ME (1985) The generation of capillary instabilities on a liquid jet. J. Fluid Mech. 168:479-500

Li and Fontelos (2003) Drop dynamics on the beads-on-string structure for viscoelastic jets: a numerical study. Phys. Fluids, 15(4):922-937

Mathues W, Formenti S, McIlroy C, Harlen OG, Clasen C (2018) Caber vs ROJER –different time scales for the thinning of a weakly elastic jet. J Rheol 62(5):1135–1153

McKinley (2005) Visco-elasto-capillary thinning and break-up of complex fluids. Rheol. Rev. 3: 1-48

Merrill EW, Leopairat P (1980) Scission of non-interpenetrating macromolecules in transient extensional flows. Polym Eng Sci 20(7):505–511

Mun RP, Byars JA, Boger DV (1998) The effects of polymer concentration and molecular weight on the breakup of laminar capillary jets. J. Non-Newtonian Fluid Mech. 74(1–3):285–297

Nghe P, Tabeling P, Ajdari A (2010) Flow-induced polymer degradation probed by a high throughput microfluidic set-up. J. Non-Newtonian Fluid Mech. 165(1–3):313–322

Nguyen TQ, Kausch HH (1988) Chain scission in transient extensional flow kinetics and molecular weight dependence. J. Non-Newtonian Fluid Mech. 30:125-140

Odell JA, Muller AJ, Narh A, Keller A (1990) Degradation of polymer solutions in extensional flows. Macromolecules 23:3092-3103

Rayleigh L (1878). On the instability of jets. Proc. London Math. Soc. 10, 4–13.

Rognin E, Willis-Fox N, Zhao TZ, Aljohani TA, Daly R (2021) Laminar-flow-induced scission kinetics of polymers in dilute solutions. J. Mech Fluids 924:A24-1-26

Schümmer P, Tebel KH (1983) A new elongational rheometer for polymer solutions. J. Non-Newtonian Fluid Mech. 12(3):331–347

Sharma V, Haward SJ, Serdy J, Keshavarz B, Soderlund A, Threlfall-Holmesf P, McKinley GH (2015) The rheology of aqueous solutions of ethyl hydroxy-ethyl cellulose (EHEC) and its hydrophobically modified analogue (hmEHEC): extensional flow response in capillary break-up, jetting (ROJER) and in a cross-slot extensional rheometer. Soft Matter 11:3251-3270

Stelter M, Brenn G, Yarin AL, Singh RP, Durst F (2000) Validation and application of a novel elongational device for polymer solutions. J Rheol 44(3):595–616

Stelter M, Brenn G, Yarin, AL, Singh RP, Durst F (2002a) Investigation of the elongational behavior of polymer solutions by means of an elongational rheometer. J. Rheol, 46(2), 507-527

Stelter M, Brenn G, Durst F (2002b) The influence of viscoelastic fluid properties on sprays formation from flat-fan and pressure-swirl atomizers. Atom. Sprays, 12:299-327

Tirel C (2019) Etude expérimentale de l'atomisation de structures ligamentaires viscoélastiques. Thèse de Normandie Université, 2 avril 2019

Tirel C, Renoult MC, Dumouchel C (2020) Measurement of extensional properties during free jet breakup. Exp Fluids, 61:21

Thiesset F., Dumouchel C., Ménard T., Aniszewski W, Vaudor G, Berlemont A (2019) Probing liquid atomization using probability density functions, thevolume-based scale distribution and differential geometry. ILASS-Europe 29th, 2-4 September 2019 Paris, France

Vadillo DC, Mathues W, Clasen C (2012) Microsecond relaxation processes in shear and extensional flows of weakly elastic polymer solutions. Rheol. Acta 51, 755-769

Yarin AL (1993) Free liquid jets and films: hydrodynamics and rheology. Longman Scientific and Technical and Wiley and Sons, New York

Yon J, Lalizel G, Blaisot JB (2004) A statistical morphological determination of the growth rate of the interfacial disturbance of an excited Rayleigh jet. Journal of Flow Visualization & Image Processing, 11:1-17